Dissertation

submitted to the
Combined Faculties for the Natural Sciences and for Mathematics
of the Ruperto-Carola University of Heidelberg, Germany
for the degree of
Doctor of Natural Sciences

presented by
Diplom-Physikerin Katrin I. Willig
born in Künzelsau

Oral examination: February 16th, 2006

# STED microscopy in the visible range

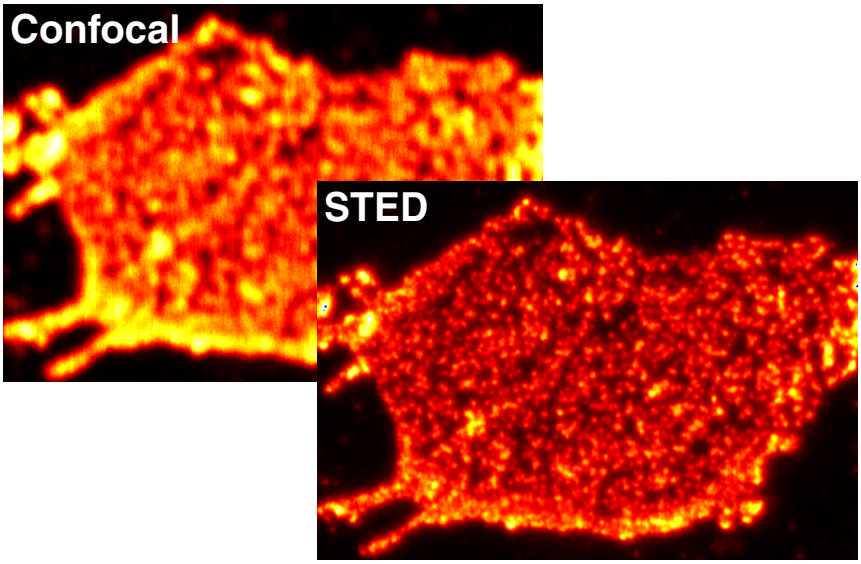


Referees: Prof. Dr. Stefan W. Hell
Prof. Dr. Josef Bille

**Abstract**
Light microscopy is a key scientific instrument in the life sciences. However, the resolution of far-field light microscopy is limited by diffraction. Exploiting a saturated depletion of the molecular excited state by stimulated emission, stimulated emission depletion (STED) breaks the resolution barrier in the important subfield of fluorescence microscopy. To this end, STED microscopy utilizes a doughnut-shaped beam featuring a central zero which is capable of quenching the fluorescence solely in the focal periphery. While STED microscopy was initially restricted to near infrared-emitting fluorophores, in this thesis STED microscopy is shown to be viable with visible (green-yellow-red) fluorophores. In particular, STED is established with the green and yellow fluorescent proteins (GFP, YFP) which are endogenous cellular markers of outstanding biological importance. The spectral conditions for STED with these fluorophores are given. The expansion of STED to the visible range has enabled the first application to biophysics and to addressing unsolved problems of cell biology. For example, STED microscopy revealed that the synaptic vesicle protein synaptotagmin remains an integral patch following fusion with the plasma membrane. Moreover, membrane microdomains were resolved with unprecedented (65 nm) spatial resolution. Furthermore, a novel doughnut-shape of the STED beam utilizing a helical phase ramp and a central singularity was established for STED. Finally, due to the smaller wavelength for stimulated emission, the viability of STED with visible dyes pushes the resolution down to smaller attainable values.

**Zusammenfassung**
Die Lichtmikroskopie ist ein wichtiges Instrument in den Biowissenschaften. Die Auflösung in der Fernfeld-Mikroskopie ist jedoch beugungsbegrenzt. Die Entvölkerung des angeregten molekularen Zustands durch stimulierte Emission, *stimulated emission depletion* (STED) wird verwendet, um die Auflösungsgrenze in der Fluoreszenzmikroskopie zu überwinden. Dazu wird in der STED Mikroskopie ein ringförmiger Strahl mit einer Nullstelle im Zentrum benutzt der die Fluoreszenz in der Peripherie des Fokus löscht. Während STED Mikroskopie anfangs auf infrarot emittierende Fluorophore beschränkt war, wird in dieser Arbeit gezeigt, dass diese Methode auch mit sichtbaren Farbstoffen (grün - gelb - rot) möglich ist. Besonders interessant ist die Einführung der grün und gelb fluoreszierenden endogenen Proteine (GFP, YFP), die von außerordentlicher Wichtigkeit in der Biologie sind. Die spektralen Bedingungen für STED an diesen Proteinen werden hier angegeben. Die Ausdehnung von STED auf den sichtbaren Wellenlängenbereich ermöglicht erste Anwendungen in der Biophysik und erlaubt das Herangehen an ungelöste Probleme in der Zellbiologie. Zum Beispiel hat die STED Mikroskopie aufgedeckt, dass Synaptotagmin, ein synaptisches Vesikelprotein, nach der Verschmelzung mit der Membran lokalisiert bleibt, statt zu diffundieren. Darüber hinaus werden Membranmikrodomänen mit bisher beispielloser räumlicher Auflösung (65 nm) aufgenommen. Im weiteren wurde eine neue Doughnutform für den STED Strahl benutzt. Darüber hinaus ermöglicht die kürzere Wellenlänge des sichtbaren STED Lichts kleinere erreichbare Auflösungen.

# Abbreviations

| | |
|---|---|
| 1-D | one-dimensional |
| 2-D | two-dimensional |
| 3-D | three-dimensional |
| CLSM | confocal laser scanning microscope |
| conf | confocal |
| Dnm1p | dynamin-related protein in yeast |
| exc | excitaion |
| EM | electron microscopy |
| FCS | fluorescence correlation spectroscopy |
| FFS | fluorescence fluctuation spectroscopy |
| FIDA | fluorescence intensity distribution analysis |
| FISH | fluorescence *in-situ* hybridization |
| FLIM | fluorescence lifetime imaging |
| FWHM | full width at half maximum |
| FRAP | fluorescence recovery after photobleaching |
| FRET | Förster resonance energy transfer |
| GFP | green fluorescent protein |
| ICS | image correlation spectroscopy |
| LCD | liquid crystal display |
| MPM | multi photon microscopy |
| PAL-SLM | parallel-aligned nematic liquid crystal spatial light modulator |
| PBS | phosphate buffered saline |
| PSF | point-spread-function |
| SNARE | soluble N-ethylmaleimide-sensitive factor attachment protein receptors |
| SNAP-25 | synaptosome associated protein of 25 kDa |
| STED | stimulated emission depletion |
| TEM | transmission electron microscopy |
| OPO | optical parametric oscillator |
| VLP | virus-like particle |
| $\odot$ | convolution |
| $\otimes$ | correlation |

# Contents


**1 Introduction** **1**
- 1.1 Light microscopy in cell biology . . . 1
- 1.2 Modern visible light microscopy techniques . . . 4
- 1.3 Principles of STED . . . 6
- 1.4 Towards STED applications in biology . . . 9

**2 Advances in the STED technique** **11**
- 2.1 STED setup . . . 11
  - 2.1.1 STED: doughnut shaped focal spot . . . 12
  - 2.1.2 The microscope's imaging capability . . . 14
- 2.2 New fluorescent markers for STED in the visible range . . . 16
  - 2.2.1 A yellow-green emitting organic dye . . . 16
  - 2.2.2 The green fluorescent protein - a biological marker . . . 17

**3 Applications of STED with a visible dye** **19**
- 3.1 Membrane microdomains . . . 20
  - 3.1.1 Microdomains of fusion proteins imaged by STED . . . 21
  - 3.1.2 Microdomain ensemble analysis by methods of fluctuation spectroscopy . . . 25
  - 3.1.3 Syntaxin clustering by protein-protein interaction . . . 34
- 3.2 Synaptic vesicles before and after fusion . . . 38
- 3.3 Microtubules . . . 45
- 3.4 Colloidal crystals . . . 46

**4 STED on the green fluorescent protein (GFP)** **49**
- 4.1 Introduction: GFP - a widely used biological marker . . . 49
- 4.2 GFP - a label for STED microscopy . . . 49
- 4.3 Size distribution of Dnm1p-GFP, a mitochondrial fission protein in yeast . 52

**5 Conclusion and outlook** **57**

**Bibliography** **59**

**A Appendix** **66**
A.1 Membrane microdomains: material and methods . . . . . 66
A.2 Synaptic vesicles . . . . . 67
A.2.1 Simulation of patched synaptic vesicles . . . . . 67
A.2.2 Material and methods . . . . . 67
A.3 Microtubules: material and methods . . . . . 68
A.4 Synthesis of colloidal particles . . . . . 68
A.5 Miscellaneous . . . . . 68

**Acknowledgment** **69**

# 1 Introduction

## 1.1 Light microscopy in cell biology

Light has been one of the most essential factors for the evolution of life. In the beginning bacteria developed photosynthesis to harvest the energy of sunlight. Then, photosynthesis became the basis for the evolution of plants which use chlorophyll to synthesize metabolites which at the same time, enrich the atmosphere with oxygen. A basis for modern life was thus provided. Visible light is therefore in principle compatible with any kind of live cells, at least at moderate intensities. The life compatibility of light allows one to build microscopes which use visible light as the only possible probe known to study live cells and learn about their fundamental functions.

**History:** The term cell was coined by Robert Hook in 1665 (*Micrographia*). He used a primitive microscope to look at cells of cork tissue. However, the advent of cell biology came 200 years later when Schwan and Schleiden systematically started to study mammalian and plant cells. They were the first to establish a fundamental cell theory stating that every cell originates from the splitting of an already existing cell. This idea was highly controversial at those times as it implied that life can only arise from other life [1]. At about the same time the development of microscopes experienced its first summit. In 1846, Carl Zeiss started to produce microscopes in Jena. When he noticed that for further optimization a fundamental theory was necessary he engaged the young scientist Ernst Abbe. In 1873, Abbe derived the wave theory of microscopic imaging [2]. Its most famous result is that the resolution of a microscope is limited by diffraction and therefore cannot be made arbitrarily small. In his theory, the limitation of the lateral spot size is described by the following equation: $\Delta x = 0.5\lambda/NA$, with $\lambda$ being the wavelength and $NA = n \sin \alpha$ the numerical aperture. The refractive index $n$ and the focusing angle $\alpha$ are subject to technical limitations. Hence only structures of at least 200 nm size can be resolved by light microscopy. Abbe's theory was a major breakthrough and remains one of the most fundamental theories in the history of optical microscopy. Together with Otto Schott, a chemist who was responsible for the development of improved glass formulas, Abbe and Zeiss developed and manufactured the finest microscopes of their time. However, for a long period of time, no fundamentally new developments in light microscopy emerged.

**Electron microscopy (EM):** At the end of the 1920s, Ernst Ruska, a student at the Berlin Technical University, started to develop magnetic lenses to control electron beams, which

was the beginning of the development of electron microscopy. As the de Broglie wavelength of electrons can be below 1 nm, it offers a superior resolution down to the molecular scale [3]. Unfortunately, highly energetic electrons are inherently destructive for biological material and therefore can not be used to study live cells. Moreover, because electron microscopes are evacuated, sample preparation is elaborate. The samples must be fixed, be embedded in epoxy and for a better contrast, be enriched with heavy metals. In a transmission electron microscope (TEM), only thin slices of about 30-100 nm thickness can be used such that the electrons can penetrate through the slice. Despite all these disadvantages, TEM is up to now widely used in structural biology and images are ubiquitous in every textbook of cell biology because of its superior resolution [1].

Although the technique has been used for decades and microscopes are commercially available, new developments are currently emerging. In the last few years electron tomography was introduced with a resolution of 2-10 nm in three dimensions. Here, the sample is rotated and many transmission images are taken at various angles. The structure can then be reconstructed by numerical algorithms [4, 5]. Other promising results have been achieved by improving the labeling techniques. Commonly, proteins are stained by antibodies marked with colloidal gold [6]. This is very inefficient as only a few immunogold antibodies may be within the thin slice. In a new approach, proteins of interest are fused genetically to a sequence motif Cys-Cys-Pro-Gly-Cys-Cys (where Cys is cysteine, Pro is proline and Gly is glycine) which is then specifically labeled with a biarsenical derivative of the red fluorophore resorufin termed ReAsH [7]. This procedure has two advantages. First, the dye is fluorescent; that is the cell can be imaged alive in a fluorescent microscope. Second, under strong illumination, the fluorophore catalyses oxidation of daminobenzidine (DAB) which results in a electron dense precipitate increasing the contrast of the EM image. A proof of principle is already published [7] whereas the technique is not yet widely used since the biarsenical compound is very unstable. In the future, this method could combine the high resolution of the electron microscope with dynamical information of live cell imaging. However, EM will always remain a very time consuming and elaborate technique.

**Biological markers:** Despite light microscopy having inferior resolution, it has remained the most popular imaging technique in biology. As there is no need for elaborate sample preparation, images can be recorded within minutes. The wide range of available markers adds to the importance of light microscopy in biology. A cell contains thousands of different proteins and many lipids, varying in structure and function. Most biological studies nowadays are targeted towards a deeper understanding of the structures, the functions and the interactions between these proteins and lipids. These studies require the localization and dynamics of specific proteins which, in turn, requires selective labeling strategies. The first approach for specific labeling was the development of the fluorescent antibody technique in the 1940s. Antibodies bind very specifically to proteins and can be decorated with fluorescent dyes. Immunolabeling is still a very common technique in biology despite not being live cell compatible. A further breakthrough was the development of fluorescent *in-situ* hybridization (FISH) in the 1980s. With this technique, special

parts of the DNA can be labeled and therefore be localized on the chromosome [8]. In 1992, the cloning of the green fluorescent protein (GFP) introduced a paradigm shift in cell biology [9]. From now on, fluorescent proteins could be fused virtually to any other protein, providing that the target protein remains functional. The GFP information can even be incorporated in the genome of cell lines or whole animals, meaning that these cells express thereafter only protein chimera instead of the protein of interest while the cell is alive and splitting. In the last decade, a whole new bunch of proteins was created by mutagenesis with each of them having a different spectroscopic feature or chemical sensitivity [10, 11].
For some applications, the rather large size of the GFP (2 nm by 4 nm) is perturbing. Therefore a binding concept for a small chromophor was developed along the lines of ReAsH in EM. A receptor domain of four cystein molecules is genetically introduced into the protein. This receptor site can bind biarsenical ligands which in turn can be linked to fluorescent molecules. The most common ligand is FLASH (fluorescein arsenical helix binder) [12]. This technique is capable of labeling proteins in live cells and at different positions within the protein. However, the fluorophore is very unstable and the necessary arsenic compound is very toxic.

**Innovative uses of light microscopy:** Over the years, many techniques evolved which are based on light microscopy. They use either unique properties such as resonance energy transfer to determine relative protein locations far below the diffraction limit or, on the other hand, fluorescence fluctuations, single particle tracking or simply bleaching to reveal information about protein dynamics. In the following, these methods are shortly introduced [13].
Förster Resonance Energy Transfer (FRET) is based on the nonradiative energy transfer from an electronically excited donor molecule to an acceptor molecule via dipole-dipole coupling [14]. Spectrally, an overlap of the donor emission and acceptor absorption is required for an energy transfer. There are two methods to detect energy transfer. Either the spectrally resolved fluorescence is detected and analyzed for the ratio of donor and acceptor fluorescence or by measuring the lifetime of the donor fluorescence, which will be reduced upon energy transfer [15]. The transfer rate varies with the $6^{th}$ power of the donor-acceptor separation ($r^{-6}$) over the range of 1-10 nm. Therefore this technique is sensitive to molecular conformation and separation on a range of a few nanometer. FRET can be detected either in-vitro or spatially resolved in the cellular environment by imaging.

Another light microscopy based method is single particle tracking (SPT). This technique is especially suited for following the movement of membrane proteins or lipids with a spatial accuracy of just a few to tens of nanometers. The particles to be observed are bound to colloidal gold or fluorescent markers like quantum dots or GFP. It should be realized that the localization of particles must not be confused with resolution. Resolution means that a microscope cannot separate two points closer together than the full width at half maximum (FWHM) of their intensity spot size (Rayleigh criterion). However, the localization accuracy of sparse particles can be of the order of nanometer assuming a suf-

ficient signal-to-noise ratio.
Information on local concentrations and the diffusion constants of proteins in live cell membranes are often obtained by fluorescence correlation spectroscopy (FCS) [16]. It detects the fluorescence intensity variations when proteins or protein clusters labeled with fluorescent markers are diffusing through the focal volume. Translational mobility information can also obtained by FRAP which stand for fluorescence recovery after photobleaching [17]. First, an area of a cell is bleached by high laser intensities. Then the fluorescence recovery is observed by taking several images in a row.

## 1.2 Modern visible light microscopy techniques

**Confocal Microscopy:** The confocal light microscope invented by Minsky in 1955 [18] has become very popular in biology and is even indispensable for some methods, like for instance FCS. The main feature of a confocal microscope compared to a widefield microscope is its optical sectioning ability. It allows one to image thick translucent objects without the presence of out-of-focus blur from surrounding planes [19].

As already mentioned in the introductory section, light focused by a lens is diffraction limited due to the wave nature of light, i.e. a point-like light source cannot be imaged to a point again but is rather spread out. The intensity distribution $h(\mathbf{r})$ of this spreading is called intensity *point-spread function* (PSF). It consists of a pronounced central main maximum surrounded by side maxima of much less intensity. The intensity distribution in the focal plane (=lateral distribution) has circular symmetry whereas it is at least three times more elongated along the optical axis (=axial). The lateral spot is often referred to as Airy disc which is defined as the lateral distance between the primary intensity minima. The diameter of the Airy disk as already mentioned in the introduction, is given by:

$$\Delta x, \Delta y = 1.22 \frac{\lambda}{NA} \tag{1.1}$$

The same criterion can be used to define the axial resolution. Here, the distance between the primary minima is [20]:

$$\Delta z = 4.00 \frac{n\lambda}{(NA)^2} \tag{1.2}$$

However, one should keep in mind that the light is only bundled in the focal plane whereas the energy integrated over lateral planes is remaining constant in front of, in or behind the focal spot. This results in an unstructured but intense background signal. In a confocal microscope, yet, a point-like detection is added. As the light path can be reverted, the detection pinhole acts as if it were imaged into the sample. That means that only these photons originating from this detection volume are detected with a probability distribution $h_{\,\mathrm{det}}(\mathbf{r})$. Therefore the effective PSF $h_{\,\mathrm{eff}}(\mathbf{r})$ is given by the product of the excitation PSF $h_{\,\mathrm{exc}}(\mathbf{r})$ and the detection PSF $h_{\,\mathrm{det}}(\mathbf{r})$:

$$h_{\,\mathrm{eff}}(\mathbf{r}) = h_{\,\mathrm{exc}}(\mathbf{r}) h_{\,\mathrm{det}}(\mathbf{r}) \simeq h^2_{\,\mathrm{exc}}(\mathbf{r}) \tag{1.3}$$

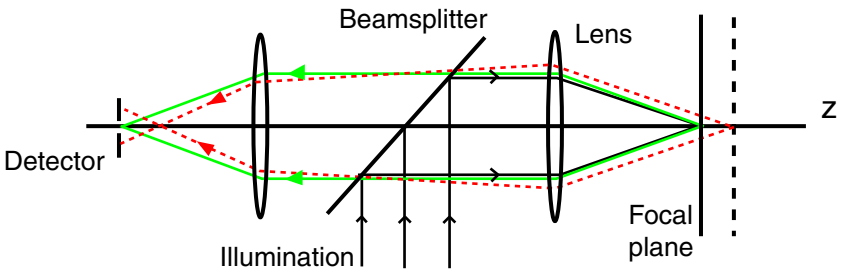


**Figure 1.1:** Optical sectioning capability of a confocal microscope [20]

In theory the intensity distribution $h(\mathbf{r})$ is described by Bessel functions but very often it is approximated by a Gaussian distribution. Hence, the full-width at half-maximum (FWHM) is used to characterize the resolution of the microscope.
Fig. 1.1 shows an illustration of the confocal sectioning capability of an (epi-)fluorescence microscope. The illuminating laser light is focused by an objective lens into the sample. The fluorescence is collected by the same lens and focused onto a detector. It is obvious that the excitation and detection spots must be overlapped carefully for proper function. For image acquisition, the sample has to be moved through the focal spot. While the confocal microscope introduces optical sectioning, its resolution improvement is not large. For point-like pinhole, the FWHM would be decreased 1.4 fold (for same wavelength of excitation and detected fluorescence). In practice it is between 1 and 1.4 fold, depending on the size of the pinhole which is a trade-off between signal intensity and resolution.
A milestone in confocal microscopy development was the introduction of the confocal laser scanning microscope (CLSM) in the 1980s [21]. Lasers became readily available and were from then on used as high intensity excitation sources. In CLSM, scanning of the beam instead of the specimen led to a faster acquisition time and less artifacts due to vibration.

**4Pi microscope:** Recapitulating, the PSF of a (confocal) light microscope in the axial direction is significantly larger than its lateral counterparts due to the asymmetry in focusing. The focusing angle of an objective lens is technically limited to about 70°. If it could be increased to the full solid angle of $4\pi$, the focal spot would be spherically symmetric. This condition can be approximated by fusing the apertures of two opposing lenses by interference, the so-called 4Pi microscope [22, 23]. Constructive interference in the focal point results in a pronounced intensity maximum that is about four times narrower than that of a single lens. The axial resolution can even be further enhanced with coherent detection. Its applicability to live cells with an axial resolution of 80 nm was shown in [24]. Meanwhile, a commercial version of the 4Pi microscope has become available (Leica, Mannheim, Heidelberg).

**Surface methods:** Total internal reflection (fluorescence) microscopy (TIRFM) is another technique to reduce the extent of the PSF in the axial direction. Here the coverglass

sample interface is illuminated at a high angle such that total reflection occurs and an evanescent field is established. Since the evanescent field has a penetration depth of about 100 nm only signal from a very thin layer is detected. TIRFM is often used in biology to study processes related to the plasma membrane.
Another way to overcome diffraction is to confine the light sample interaction to an ultra sharp aperture of 20 to 200 nm diameter and to avoid focusing altogether. This is the basic idea of near-field scanning optical microscopy (SNOM). The disadvantage is that this approach is confined to surfaces. Moreover, the tip must be scanned parallel to the sample surface at a short distance of less than 100 nm which is technically demanding but was demonstrated to be sensitive to single molecules on living cells [25].

**Multiphotonabsorption/Scattering:** Non-linear effects in the focal area are used to confine the PSF size. For instance, in multiphoton microscopy (MPM), only fluorochromes are excited by absorption of more than one photon [26]. The sum of the photon energy of the two or more photons must fit to the excitation of the fluorochrome. This process is only effective at the center of the focused beam where the photon density is high. In general, this has no real effect on the resolution. Indeed, the quadratic effect narrows the PSF but this is more than compensated by the doubled excitation wavelength necessary for two photon absorption. The advantage of MPM is that the non-linear excitation results in a good sectioning capability in thick specimen without background light and without the need of a confocal pinhole [27]. Non-linear imaging also includes second- or third-harmonic generation or a more complex form, namely coherent anti-Stokes Raman scattering (CARS) [28].

## 1.3 Principles of STED

It was explained before that the size of a focal spot in a light microscope will always be limited by diffraction due to a fundamental physical limit. It can be expanded by techniques like for example the 4Pi microscope but it cannot be broken as it is always constricted by the wavelength of the visible light. Stimulated emission depletion (STED), however, is a recently developed approach to overcome the diffraction barrier and increase the resolution up to the molecular scale [29, 30, 31]. In the following the STED concept will be explained briefly. For details see the literature [32, 23].
In a spot scanning fluorescence microscope, the lateral resolution is determined by the spatial extent of the fluorescing area, which in turn is equal to the excitation area $h_{\mathrm{exc}}(\mathbf{r})$ (if the excitation is not saturated). Any process which inhibits the fluorescence in the periphery and confines the fluorescence to the inner region of the PSF leads to a smaller fluorescing volume and therefore enhances the resolution. As the term STED indicates, light is used to deplete the excited fluorescent molecule before it can fluoresce. Fig. 1.2 shows the energy levels involved in the excitation and emission of a fluorescent molecule. $S_0$ and $S_1$ are the ground and first excited singlet states, respectively. $S_0^{\mathrm{vib}}$ and $S_1^{\mathrm{vib}}$ are higher vibrational levels of these states. According to the Franck-Condon principle [33],

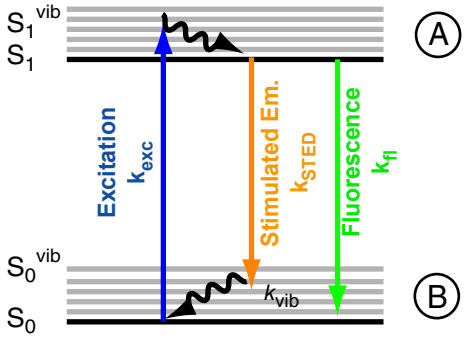


**Figure 1.2:** Jablonski diagram: Energy states of fluorescent molecule

the molecule can be excited from the ground state $S_0$ to the first excited state $S_1^{\text{vib}}$ by light if the photon's wavelength matches the energy gap between $S_0$ and $S_1^{\text{vib}}$. Fluorescence (spontaneous emission) is described as radiative relaxation $S_1^0 \rightarrow S_0^{\text{vib}}$ and can be induced by light (stimulated emission). The excited state can be depleted completely because reexcitation can be neglected as the vibrational relaxation $S_0^{\text{vib}} \rightarrow S_0$ is of the order of subpicoseconds which is very fast. For the sake of simplicity higher electronic singlet states and triplet states are neglected.

The rate of the fluorescence $k_{\text{fl}}$ is related to the probability for spontaneous emission and is given by the inverse of the lifetime $1/\tau$. The time window during which stimulated emission can be applied is limited by the excited state lifetime and is of the order of nanoseconds for organic molecules. The rates for excitation and stimulated emission are given by the product of the molecular cross section $\sigma$ and the photon flux $h$; hence, $k_{\text{exc}} = \sigma_{\text{exc}} h_{\text{exc}}$ for excitation and $k_{\text{STED}} = \sigma_{\text{STED}} h_{\text{STED}}$ for stimulated emission. The cross section is a molecule specific entity. Therefore STED depends strongly on the spectroscopic properties of the fluorophore being used.
Mathematically, the dynamic behavior of the four states $S_0$, $S_1$, $S_0^{\text{vib}}$ and $S_1^{\text{vib}}$ can be described by a system of four differential equations. As stimulated emission is the basic idea of laser operation, the respective equations can be found in several textbooks. With some approximations for the boundary conditions and the temporal shape of the excitation and emission pulses, the differential equations can be solved [32]. It was shown [34] that by the time the STED pulse has vanished, the population of the $S_1$ state can be approximated by

$$N_{S1} \approx N_0 \, exp(-\sigma_{\text{STED}} h_{\text{STED}}) = N_0 \, \eta(h_{\text{STED}}) \tag{1.4}$$

where $N_0$ is the population immediately after excitation. The initial population is reduced by a factor of $\eta$, the depletion factor. In some contexts, the deexcitation probability or saturation function $\epsilon$ is used which is given by $(1 - \eta)$. The strong optical nonlinearity implied by this exponential dependence of the fluorescence on the fluence of the STED pulse is the key to significantly overcoming the diffraction limit.
To summarize, the depletion efficiency strongly depends nonlinearly on the light intensity and is temporarily restricted to a time window after excitation within the lifetime of the fluorescent state. Therefore it is much more efficient and in most cases mandatory, to use

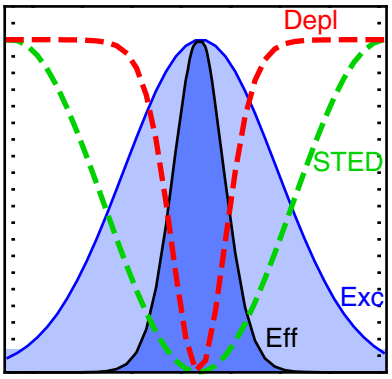


**Figure 1.3:** Breaking the diffraction barrier by STED. Normalized intensity profile of the Excitation PSF $h_{\mathrm{exc}}$, STED PSF $h_{\mathrm{STED}}$, Depletion probability and Effective PSF $h_{\mathrm{eff}}$

pulsed excitation and depletion instead of continuous illumination. Both pulses then have to be correlated in time in a way that the STED pulse is coming right after the excitation. It was shown previously that a pulse length of approximatelly 150 ps is optimal for STED microscopy [35]. Shorter pulses lead to higher photodamage of the dye whereas pulses longer than the fluorescence lifetime of the dye would result in incomplete fluorescence depletion.

To exploit fluorescence suppression as a tool for resolution enhancement, the microscope has to be extended for a second color. In general, a STED microscope can be described as a two color confocal microscope (compare Fig. 1.1). The confocal pinhole is optional for the three-dimensional sectioning ability whereas it has little effect on the effective spot size. Crucial for the STED microscope is the shape of the STED PSF. To achieve resolution enhancement, the STED focus has to be engineered to provide a zero-intensity minimum in the geometrical center and high intensities in the focal periphery. Thus, only molecules in the center of the excitation PSF are fluorescing, molecules in the outer areas are quenched by the STED light.

Several methods are conceivable to design a STED PSF with a zero in the center. They all have in common that the phase of a part of the beam is altered spatially in a way to obtain destructive interference in the center of the focus and constructive interference in some parts of the periphery. For a demonstration of the technique, the STED focal intensity profile $h_{STED}$ is approximated by a $\cos^2$ distribution in Fig. 1.3. As the STED focal spot is limited by diffraction as well and the shape is result of an interference pattern, the FWHM of its maximum (or minimum, respectively) is about equal to the FWHM of the diffraction limited spot of the unmodulated beam. For the simulation an intensity of $I = 10I_{sat}$ ($I_{sat}$: drop of fluorescence to 50%) for the STED distribution $h_{\mathrm{STED}}$ was chosen.

The theoretical probability distribution for depletion can be calculated by $(1-\eta(I_{\mathrm{STED}}/I_{\mathrm{sat}}))$. A profile is shown in Fig. 1.3. The gap between the maxima of the depletion distribution is clearly more narrow than for the STED intensity profile alone. The consequence is a pronounced narrowing of the effective PSF.

The resulting spot size can be shown to be given by [31]:

$$\Delta x \approx \frac{\lambda}{2n \sin \alpha \sqrt{1 + I/I_{sat}}} \tag{1.5}$$

which is very similar to Abbe's equation of resolution. At the saturation intensity $I = I_{\mathrm{sat}}$, the fluorescence has dropped to $1/e$ of the undepleted fluorescence. For increasing STED illumination intensity, the spot size decreases continually, following a square root law. Hence the spot size is not limited any more by diffraction.

It should be mentioned that the technique of breaking the diffraction limit is not restricted to the STED principle. It can be generalized to the assumption of two arbitrary states of the fluorophore A and B [30]. One of these states must be fluorescent and one of the reversible transitions, either A→B or B→A must be a saturable optical transition. For STED, for instance, the ground state of the fluorescent molecule $S_0$ refers to a non-fluorescent state B and the excited state $S_1$ to the fluorescent state A (compare Fig. 1.2). A further concept, which is not yet implemented, is the depletion of the ground state by pumping the dye into the (non fluorescent) triplet state [36]. Moreover, a very recently published concept introduces and demonstrates that a reversibly photoswitching protein can be utilized for microscopy beyond the diffraction limit [37]. There are however still some problematic aspects of this technique like a high cross-talk between the on and off-switching and slow switching times. But as it is based on the same concept, it could become an alternative to STED for some applications.

## 1.4 Towards STED applications in biology

The concept of STED was proposed by Hell and Wichmann in 1994 [29]. Five years later, the first experimental result was published by Klar and Hell [38]. It showed a slight increase in lateral resolution from 150 nm to 106 nm just by using two offset beams (of different wavelength). Shortly after that they published a pronounced 6-fold axial reduction and 2-fold lateral reduction resulting in an approximately spherical shape of the effective PSF of 90 to 110 nm size. Moreover, a 3-fold resolution enhancement was shown on membrane-labeled bacteria E. coli and a small confinement of vacuolar membranes of live yeast cells. Thereafter, the earlier developed 4Pi microscope was combined with STED [39]. While the 4Pi microscope was set to destructive interference in the center, the constructive interference maxima before and after the focal plane were used to quench the fluorescence. A dramatic axial resolution of 33 nm ($\lambda/23$) was demonstrated on dye monolayers and membrane labeled bacteria. Then, a respective record in lateral resolution was established [31] where single fluorescent molecules were utilized as probes to prove the spatial extend of the effective PSF of 16 nm in one lateral dimension. With a combination of two beams and two phase plates, a lateral spot size of $50 \times 50$ nm was obtained. For the single molecule experiment the very photo stable dye Ja26 was used, however, this dye is not suitable for biological staining as it has no functional group.

For all these experiments, a mode-locked Titanium-Sapphire (Ti:Sa) laser was used. It was the only rugged laser which provided all the features necessary for a STED experi-

ment. It is a pulsed laser tunable over a broad wavelength range in the infrared to achieve the best STED efficiency for various dyes of various emission spectra in the infrared. The spectral width of about 10 nm is beneficial for stretching of the short, 60-100 fs pulses to up to a few hundred picoseconds by dispersion. While the Ti:Sa laser is, at least for research purposes, an appropriate choice for STED, the infrared dyes are not. Compared to the broad range available in the visible, infrared dyes are scarce. In addition, reactive derivates of infrared dyes were rare which excluded immunolabeling methods from being used. For the cell experiments mentioned above, the whole membrane was labeled with lipophilic dyes like Pyridin4 or RH414. Then the first reactive dye, MR121, was used for STED imaging. A proof of principle showing a resolution of 50 nm and images of clearly resolved immunostained tubulin fibers can be found in [40].
The dyes used up to now for STED have an emission maximum of about 680-700 nm and therefore are barely visible to the eye - a big disadvantage for optimizing biological staining procedures. Beyond that, the quantum efficiency of infrared dyes is often lower than that of visible dyes. It is obvious that some of the problems can be solved by using visible dyes. In addition, a shorter STED wavelength implies a better resolution because the spot size of the STED intensity PSF is still proportional to the wavelength (compare Eq.1.5) and interference patterns of maxima which are closer together result in smaller effective PSFs which lead to a higher reolution.
On the other hand visible light can bear some disadvantages as well. The larger photon energy of the visible light compared to that of the infrared light can, for example, induce higher photobleaching.

**This thesis shows** the first use of STED together with visible dyes for imaging biological specimen. Moreover, the most established marker used in biological applications, namely green fluorescent protein (GFP) has been made viable for to STED. Biological samples were imaged routinely to achieve first results of biological relevance with a STED microscope. Examples include the resolving of membrane microdomains with unprecedented spatial resolution of 65 nm and a study of synaptic vesicles which revealed that the synaptic vesicle protein synaptotagmin remains an integral patch following exocytosis. The applicability of GFP to STED presented here, paves the road for further and deeper insights into biological samples.

The thesis is arranged as follows. The second chapter outlines the STED setup together with a description of the novel doughnut shaped pattern of the STED focus and characterization of the imaging capability using fluorescent beads. Moreover, the spectroscopic properties of the dyes are outlined. The third chapter shows applications with the green dye Atto532: The first application is on protein clusters on membrane sheets which are immunostained; a multitude of images were recorded and evaluated by fluctuation methods. Second, a study on synaptic vesicles before and after fusion is presented. Third, immunolabeled microtubules were imaged followed by images of colloidal crystal with a fluorescent core. The last chapter presents the first images with the marker protein GFP; a recording of the size distribution of Dnm1p-GFP clusters in yeast cells.

# 2 Advances in the STED technique

## 2.1 STED setup

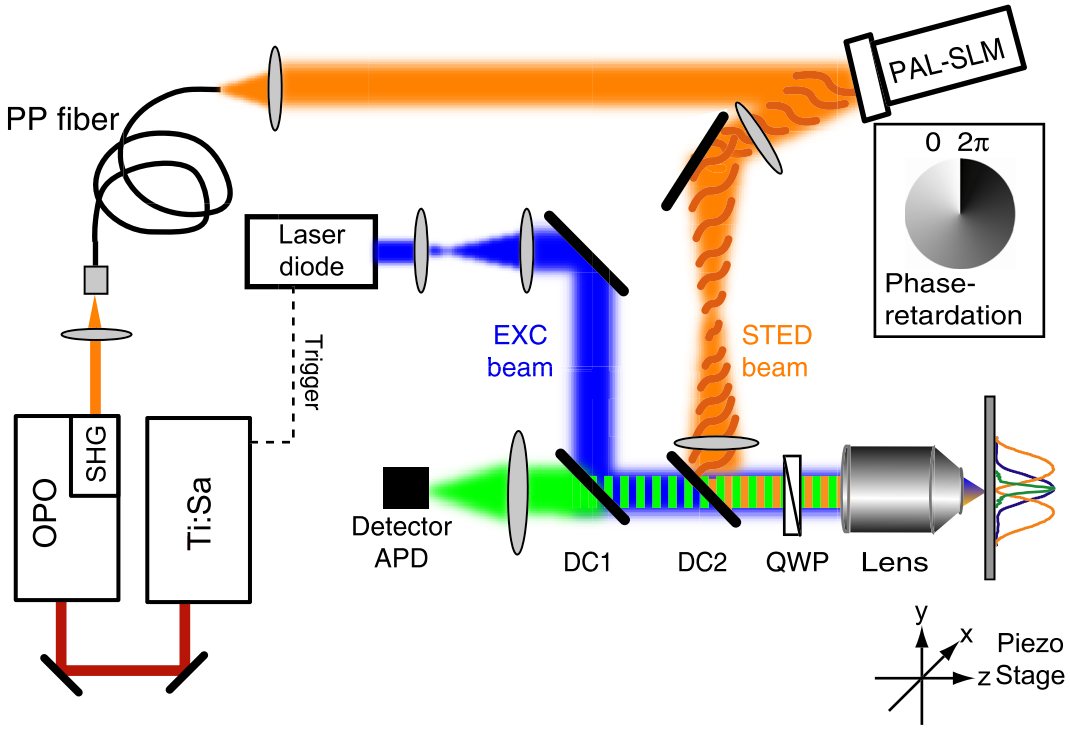


**Figure 2.1:** STED microscope. See text for explanation.

A setup with all the basic requirements of a STED microscope was developed. The main concept is outlined in Fig. 2.1.
The fluorescence excitation was accomplished with a pulsed laser diode emitting 100 ps pulses at 470 nm (Picoquant, Berlin, Germany) or at 488 nm (PicoTA, Picoquant, Germany). STED was provided by an optical parametric oscillator (OPO) (APE, Berlin, Germany) which was synchronously pumped by a mode-locked Ti:Sapphire laser (MaiTai, Spectra Physics, Mountain View, CA) operating at a repetition rate of 80 MHz. By tuning the MaiTai the OPO could be tuned from 560 nm to 660 nm. The about 200 fs pulses delivered from the OPO were stretched to a pulse length of 150-250 ps, depending on the average power, using a polarization-preserving (PP) fiber (80m, cut-off at 633 nm,

oz optics, Ottawa, Canada). The timing between the OPO and the laser diode was adjusted by a variable electronic delay (home-built) of the electric pulse coming from the MaiTai laser and triggering the laser diode. The beam conversion into a doughnut shaped beam was accomplished by means of a spatial light modulator (PAL-SLM, Hamamatsu, Hamamatsu City, Japan) delivering a helical phase ramp (0-$2\pi$) with a central singularity, imaged onto the back aperture of the objective lens. The details will be explained in the next section. Both the excitation (Exc) and the STED beams were coupled into a regular 1.4 numerical aperture oil immersion lens (HPC PL APO, 100×, Leica Microsystems, Mannheim, Germany) using two custom-made dichroic beamsplitters DC1 (DC488, Chroma Technology, USA) and DC2 (HR660nm/HT UV for STED at 615 nm and HR 640nm/HT UV for STED at 580-585 nm, Laser Components GmbH, Germany). The linearly polarized excitation and STED is turned into circularly polarized light by an achromatic quarterwave plate (QWP 460-680 nm, Bernhard Halle, Germany) in front of the objective lens. For the applied excitation and STED powers refer to the particular images in the following. The emitted fluorescence was collected by the same lens and directed onto a multimode fiber (d=$62.5\,\mu m$) which served as the confocal pinhole; the opening diameter corresponds to 71% of the backprojected Airy disc of the excitation light. The fluorescence signal was detected by an avalanche photodiode (SPCM-AQR-13-FC, PerkinElmer, OptoElectronics Europe, Germany) operating in the counting mode. The image was obtained by scanning the sample with a piezo-stage operating in the closed loop mode (Melles Griot, Cambridge, UK) at a typical pixel dwell time of 0.3 ms and a typical pixel size of 15 nm×15 nm.

### 2.1.1 STED: doughnut shaped focal spot

Up to now only binary phase retardation filters or combinations of two filters have been used to achieve a focal intensity minimum [41, 31] (apart form the 4Pi STED technique [39]). More complicated retardation patterns were not possible since these phase retardation filters consist of glass substrates partially coated with a layer of $MgF_2$ to introduce a phase retardation of $\pi$ radian.
In contrast, spatial light modulators (SLM) allow one to produce any phase retardation with a high spatial accuracy depending on the amount of pixels. In this setup, a parallel-aligned nematic liquid crystal (PAL) SLM from Hamamatsu was used [42]. It is optically addressed by a liquid crystal display (LCD) of size 1024 by 768 pixels, whereas every pixel can be independently set to a phase retardation of $0 - 2\pi$. The phase pattern on the SLM is non pixelized as the LCD is imaged to the SLM slightly out of focus. This concept avoids the drawbacks arising with standard pixelated LCDs such as diffraction on the border between the pixels. On the other hand, imaging of the SLM by an interferometer revealed that the introduced phase retardation is spatially inhomogeneous (data not shown). It may be necessary to correct for this inhomogeneity by special calibration as the irregularities in the phase retardation may introduce imperfections of the interference pattern in the focus. For STED imaging, the quality of the focal zero of the doughnut is of essential significance since the remaining STED intensity in the focus acts directly against

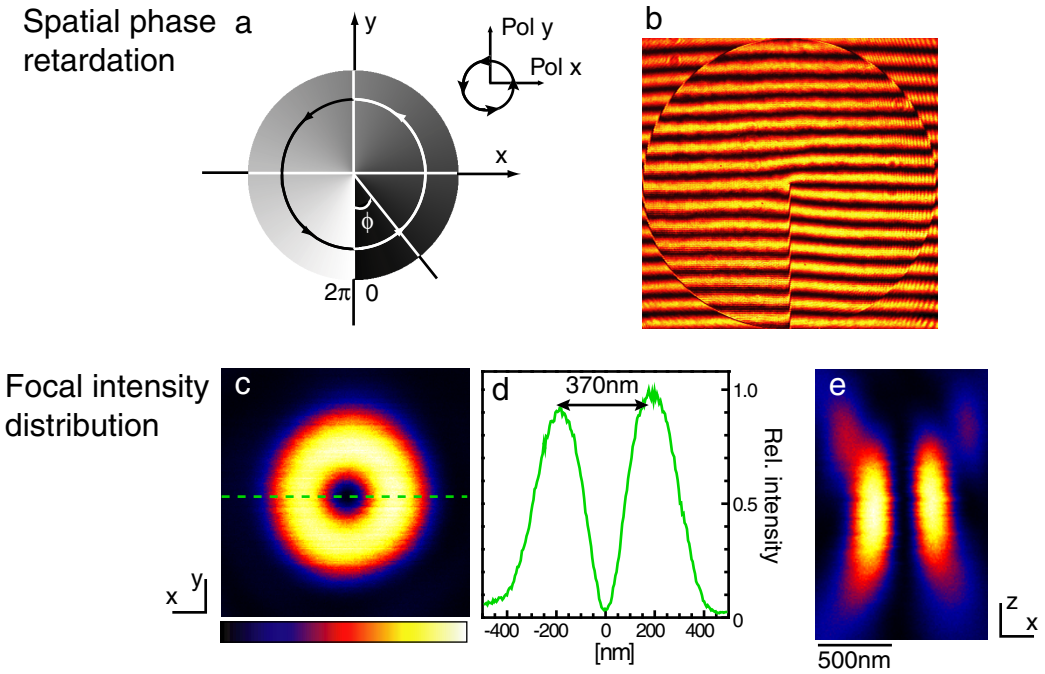


**Figure 2.2:** Focal doughnut formation. a) Helical phase ramp $(0 - 2\pi)$ applied to the PAL-SLM. b) Interferogram of the PAL-SLM while (a) is applied. c) Doughnut shape intensity distribution within the focal plane (lateral) and d) its central profile. e) Focal intensity distribution along the optical axis (axial).

the desired fluorescence confinement. Another reason for this imperfection (besides the quality of the SLM) might be aberrations induced by the optical setup. Advantageously, they can be perfectly compensated by the phase retardations applied to the SLM. Still, the quality of the zero needs to be further optimized leading instantly to a higher fluorescence signal and may also improve the resolution.

The SLM technique permits, now, to look for new and better suitable phase filters to confine the fluorescence to a narrow spot. A useful focal intensity pattern, which was recently developed, is of a doughnut shape[1] [43]. It confines the fluorescence to a small spot in the lateral plane as shown in c) of Fig 2.2. The doughnut shape results from a phase retardation of a helical phase ramp introduced to the circularly polarized light as shown in a). This phase pattern is created by the SLM; an interferogram of the SLM is shown in b). The resulting doughnut shape focal intensity distribution is shown in c). It was recorded with a reflecting gold bead of 80 nm diameter and has a diameter of about 370 nm (d). There is no effect due to the phase modulation along the axial direction as shown in e).

Previously, 2-D lateral resolution improvements were achieved by an overlay of two STED beams featuring a zero in the center and two maxima in either lateral direction [31]. However, it is inconvenient to align three beams (one excitation and two STED

[1] Simulation by Jan Keller, Department of NanoBiophotonics

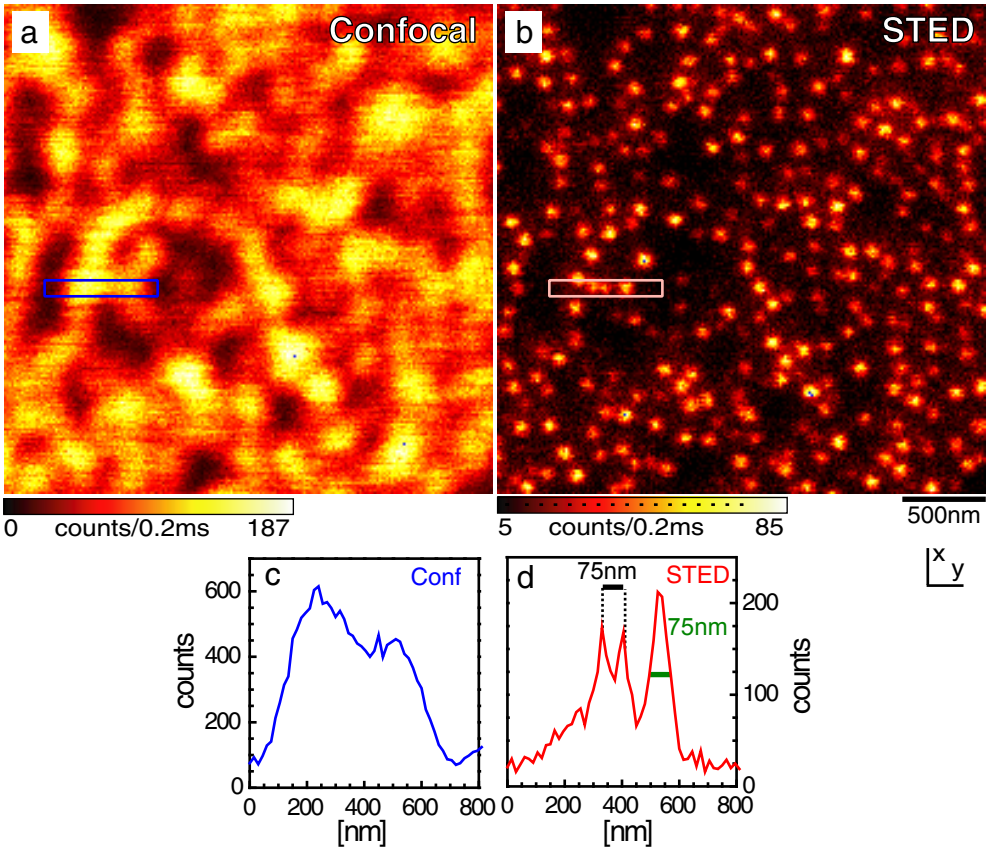


**Figure 2.3:** Images of green fluorescent beads of 40 nm diameter. Raw data of a) confocal and b) simultaneously recorded STED image. The well separated beads in a distance of 75 nm (d) demonstrate sub-diffraction resolution of $\leq$ 75 nm in the visible range and with a widely used fluorophore. c) The confocal profile shows no structure. c) and d) Sum of 4 horizontal lines as denoted in the images (a) and (b), respectively.

beams) instead of two, and on the other hand, laterally polarized light was used which preferentially depletes molecules with emission dipoles parallel to the polarization of the STED beam [34]. In contrast, the newly implemented doughnut shape shown in Fig. 2.2.c increases the resolution isotropically because of its symmetric intensity distribution and the circularly polarized light, thus independent of the lateral emission dipole distribution.

### 2.1.2 The microscope's imaging capability

After implementing the doughnut-shape focal intensity distribution into the setup, its ability to quench the excitation in the lateral periphery of the focal spot was tested. As test objects commercially available microspheres loaded with fluorescent dye were used (Yellow-green Fluospheres 505/515, Molecular Probes/invitrogen, USA). The spheres had a diameter of 40 nm and were loaded with a green emitting dye of excitation maximum at 505 nm and emission maximum at 515 nm. The beads were diluted 1:100 in $H_2O$

and sonicated for at least 10 minutes. Then, a drop was put between two coverslips and the water allowed to evaporate. The coverslip with the homogeneously distributed particles was mounted with Mowiol (see Appendix A.5) or water on a microscope slide. As only particles attached to the cover slip were imaged, the refractive index of the mounting medium did not influence the quality of the images. The sample of the yellow-green beads was then imaged in the STED microscope, images are shown in Fig. 2.3. This is the first demonstration of sub-diffraction resolution with a visible, commercially available dye in a STED microscope. The confocal image (a) shows only blurred and quite large blobs; from this, conclusions on the object's morphology can not be drawn. In contrast, the STED image (b) can reveal single, well separated small spots. They are spherical in shape as was expected for the isotropic quenching of the STED laser.
The shape of the profile of the beads (Fig. 2.3.d) shows a very sharp tip on the top and widens linearly towards the bottom. In general, the STED PSF can be well approximated by a Lorentzian curve, in contrast to the confocal PSF profile which is approximated by a Gaussian. Compared to the Gaussian, the Lorentzian becomes increasingly thinner at the top. Therefore the FWHM of the effective PSF might not be the appropriate definition for resolution of a STED microscope. In other words, assuming a Gaussian and a Lorentzian PSF of the same FWHM, the two Lorentzians can be closer together and can still be identified as two curves as opposed to two Gaussian curves. Simulations reveal (data not shown) that without noise and with a Lorentzian profile of the PSF of 65 nm FWHM, point objects can be separated down to a distance of 45 nm.
Remains the question of the resolution of the microscope. This strongly depends on the spectroscopic properties of the fluorophore like the emission cross section and the laser power, and must therefore be specifically analyzed in detail for every dye. An indication for the resolution is the spatial extent of the effective PSF. The effective PSF can only be measured with point-like objects. For extended objects, the image $imag(\mathbf{r})$ represents a convolution of the object $o(\mathbf{r})$ with the effective PSF $h_{\text{eff}}(\mathbf{r})$:

$$imag(\mathbf{r}) = o(\mathbf{r}) \odot h_{\text{eff}}(\mathbf{r}) \tag{2.1}$$

The microspheres presented in Fig. 2.3 are objects of 40 nm diameter. Simulations of a sphere of 40 nm diameter completely filled with dye convoluted with the Lorentzian distributions $h_{\text{eff}}$ of various sizes reveal that the measured spot size of $imag(\mathbf{r})$ of 75 nm (Fig. 2.3.d) corresponds to a FWHM of about 70 nm of the effective PSF $h_{\text{eff}}(\mathbf{r})$.
**Imaging conditions:** The fluospheres were excited with a laser diode at 470 nm and quenched by the STED laser at 585 nm. The average power in the focal plane was 1.1 $\mu$W for the excitation and 60 mW for the STED beam . This corresponds to a focal pulse peak intensity of 92 kW/cm$^2$ for the excitation and 4.2 GW/cm$^2$ for STED, assuming lateral a Gaussian intensity distribution and a pulse length of 100 ps and 250 ps (rectangular), respectively. The fluorescence was collected between 500 nm and 550 nm. The pixel size was 15 nm$\times$15 nm. The image was recorded simultaneously by turning the STED laser on and off after every line.

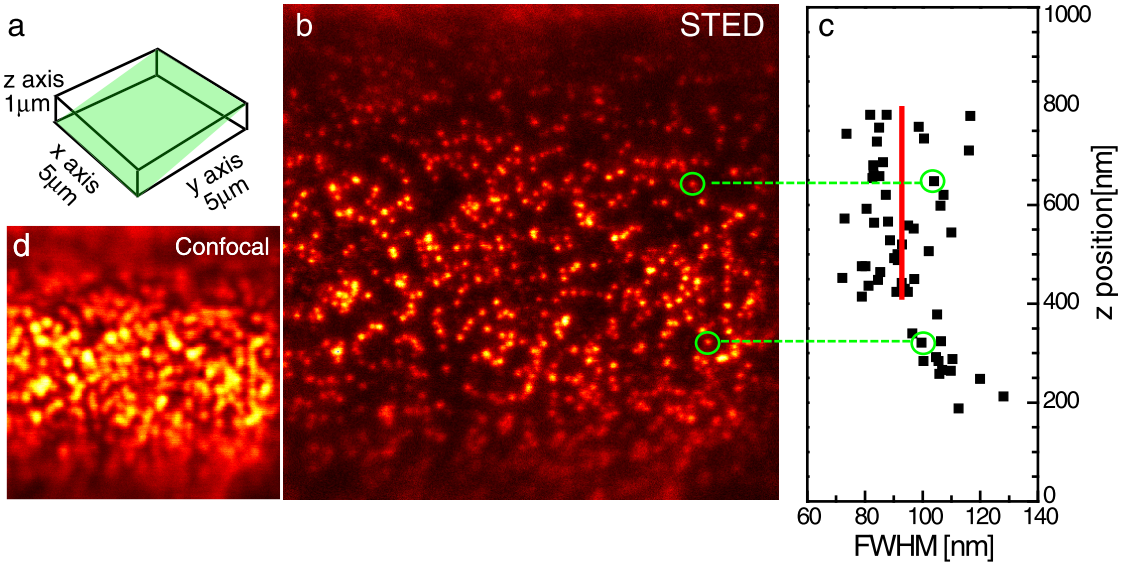


**Figure 2.4:** The STED microscope has a large depth of focus. a) Cartoon of the scanned plane, which is slightly tilted. b) STED image of yellow-green fluorescent beads at various z-positions. c) evaluation of spot sizes depending on the z-position d) Confocal control image.

**Depth of focus:** As explained previously, the doughnut mode is only quenching molecules along the lateral direction. In the z-direction it is not engineered and therefore shows the z-profile of an unmodulated PSF; it is slightly larger than the excitation PSF in the z-direction due to the longer wavelength and phase modified wavefront. It should therefore quench the fluorescence with a high depth of focus. This is demonstrated in Fig. 2.4. The image is recorded with smaller STED power than the previous image and the beads are more clustered. The figure shows an image which was taken by scanning in the x- and y-directions with a slight simultaneous shift in the z-direction. The FWHM of separated spots were then evaluated with respect to the z-coordinate, shown in c). For a broad range in z, the size distribution varies between 70 nm and 100 nm. For lower z-coordinates, the FWHM goes up to about 120 nm. For large z-coordinates, there is no decrease in the FWHM. It seems that the excitation and STED beam were not perfectly overlayed in the axial direction. However, the result demonstrates that the FWHM is relatively constant over a large range in the z-direction - at least for 400 nm as denoted in the image.

## 2.2 New fluorescent markers for STED in the visible range

### 2.2.1 A yellow-green emitting organic dye

When the decision was made to switch from the infrared to the visible range, a screening of the most important dyes was started. The screening was concentrated on functional

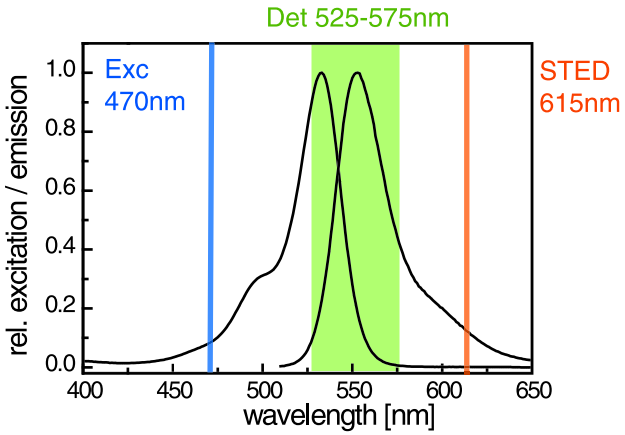


**Figure 2.5:** Excitation and emission spectrum of the green-yellow emitting dye Atto532

dyes, meaning that these dyes can be coupled to antibodies for immunolabeling. The emission of the studied dyes ranged from about 480 nm up to 600 nm and included, for example, Fluorescein, several Rhodamines, Alexa dyes (the latter is a brand name from Molecular Probes) and dyes from AttoTec. Details of the screening data are not shown here as a correct quantification is very complicate. It includes measuring of the STED depletion coefficient and photon induced damage. The challenge is that this data can vary depending on the environment or the age of the sample. However, screening of the dyes in solution for STED efficiency showed good results for two dyes, derivates of Rhodamine 6G, resulting from a cooperation with Prof. Drexhage from University of Siegen/Atto-Tec. Unfortunately the quantum efficiency of these dyes was very bad after coupling to antibodies. The absorption measurements of the coupled dyes showed that this was probably due to an aggregation of the dye molecules (data not shown). This problem was solved by a slight modification of the molecule, yielding the from now on used dye Atto532 (Atto-Tec, Siegen, Germany). The excitation and emission spectrum is shown in Fig. 2.5. This dye was proven effective in many stainings of different biological samples as can be seen in the next chapter.

### 2.2.2 The green fluorescent protein - a biological marker

The Green Fluorescent Protein (GFP) has been one of the major discoveries that has opened up new insights into biology. It has become the most widely studied and exploited fluorescence protein in biochemistry and cell biology. A real breakthrough was the cloning of the gene in 1992 [9]. Thereafter, GFP could be fused to virtually any protein of interest to analyze protein localization, movement, and chemistry in living cells [10].

GFP was discovered as a companion protein to aequorin, a chemiluminescent protein from the jellyfish *Aequorea victoria*. Fortunately the GFP after purification was fluorescent on its own upon excitation, thereby requiring no additional coenzymes for folding.

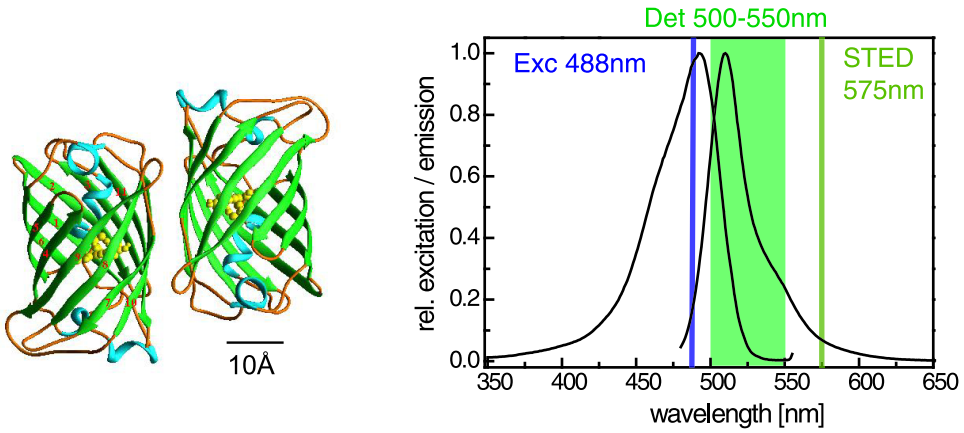


**Figure 2.6:** GFP crystal structure and fluorescence emission. a) The GFP (*wt*) protein is formed by a cylinder of eleven strands of $\beta$-sheet (green) while $\alpha$-helices (blue) cap the top and bottom. The $\beta$-*barrel* provides a scaffold for the fluorophore (yellow), which is near the geometric center. (Adapted from [44]) b) Excitation and emission spectra of the EGFP mutant used for imaging in this thesis.

The protein is very photostable due to the cylindrical structure, shown in Fig. 2.6.a, with the chromophore buried in the center. The cylinder is formed by an 11-stranded $\beta$-barrel with an $\alpha$-helix running up the axis of the cylinder. For some experiments one has to consider the rather large size of the protein of about 2 nm by 4 nm. Meanwhile GFP could be improved by mutagenesis. The wild type (*wt*-GFP), for example, could only mature at cold temperatures but not at the 37°C of mammalian cells. This could be improved by some minor but very effective mutations. Further the speed of fluorophore formation was improved to below 1 hour and the two absorbance peaks of the wild type were converted to a single absorbance peak at approximately 489 nm. Finally, the dimerisation at high concentrations was overcome. All these mutations are combined in the new enhanced version of the *wt*-GFP, called enhanced-GFP (EGFP) [45]. Fig. 2.6.b shows a normalized excitation and emission spectrum of EGFP. It can be excited efficiently with the 488 nm line of widely used Argon Ion lasers and emits green fluorescence light.

Further developments of GFP provided variants with differing excitation and emission spectra like the cyan fluorescent (CFP) and yellow fluorescent (YFP) proteins. Meanwhile also red emitting proteins are available which were extracted from other marine organisms. Of these, the DsRed from *Discosoma spec.* and HcRed from *Heteractis crispa* and their mutants, both are coral species, each with emission peaks ranging from 579 to 645 nm, have provided the most suitable red markers [11].

Summarizing, fluorescent proteins are the most widely used fluorescent probes at present. Almost any protein can be stained. A combination of various biological samples together with the high resolution from a STED microscope are of great interest.

# 3 Applications of STED with a visible dye

This chapter shows the first biologically relevant studies performed with a STED microscope. For all images the yellow-green emitting organic dye Atto532 (Chapter 2.2.1), a Rhodamine 6G derivate, was used. The first example is on membrane microdomains, an area of high research activity in biology. By the STED technique the microdomains can be better separated and therefore allows to study the microdomain distribution directly. This is not possible by a confocal microscope. For evaluation, fluorescence fluctuation spectroscopy (FFS) techniques were introduced to image analysis. The second example shows imaging by STED of the synaptic vesicle protein synaptotagmin. It reveals that the synaptic vesicle protein synaptotagmin remains clustered after exocytosis. Third, images of microtubules demonstrate the potential of the sub-resolution imaging by STED. At last, an example from nanotechnology is provided. It shows the potential use of STED microscopy in the imaging of colloidal particles, a system used, for example, to study crystal formation.

The effective PSF of the STED microscope was about 65 nm FWHM (Fig. 3.1) for all Atto532 images shown in this chapter. This corresponds to a 9-fold reduction of the focal volume with respect to the confocal spot of 195 nm FWHM (data not shown).

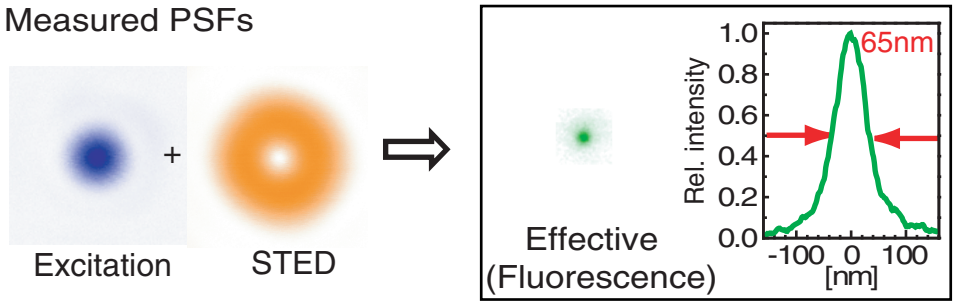


**Figure 3.1:** Measured excitation, STED and effective PSF. The excitation and STED focal spots were recorded with reflecting 80 nm diameter gold-beads. For the effective PSF point-like fluorescent probes were imaged: Primary antibodies $\leq$10 nm were spread on a coverslip and visualized with Atto532 labeled secondary antibodies. The two-dimensional distributions of excitation, STED and effective PSF are drawn to scale.

## 3.1 Membrane microdomains

Membranes are crucial for the life of a cell separating the compartments inside the cell as well as isolating the inside of the cell (cytosolic part) from the outside (plasma membrane). Membranes are formed by phospholipid bilayers in which proteins are embedded. Such proteins can, for instance, form channels through the bilayer to allow for inter- and intracellular transport. Other examples are receptor proteins, which play an important role for inter- and intracellular signaling and communication. The lipid bilayer has different constituents as well. The plasma membrane of mammals, for example, consists of various proteins, phospholipids, cholesterol, glycolipids, etc. which form a fluid system [1].

There is evidence that these lipids are inhomogeneously distributed, and that various types of specialized lipid domains play an important role in many biological processes. The characteristics of these domains, such as size, composition and dynamics, are currently under active investigation. It appears that there are many different types of membrane domains in the plasma membrane, and perhaps the entire membrane should be viewed as a mosaic of microdomains [46].

The lipid *raft* hypothesis is probably the most often discussed model of membrane microdomain formation in the last decade [47]. This theory states that the lateral organization of the plasma membrane results from liquid ordered phases which represent a preferential packing of sphingolipids and cholesterol on the outer membrane leaflet into moving platforms, so called *rafts*, into which specific proteins dissolve within the bilayer. Detergent solubilization experiments led to the discovery of detergent resistant membranes (DRMs), enriched in cholesterol, sphingomyelin and special proteins. The raft hypothesis postulates that DRMs are stabilized by cholesterol and sphingomyelin and reflect microdomains in live cells. These lipids are supposed to form liquid ordered phases in the outer membrane leaflet, in which certain proteins preferentially accumulate via their GPI-anchors (GPI: glycosylphosphatidylinositol, a glycolipid anchor). The most commonly used criterion to classify a protein as lipid raft associated is its insolubility in cold $1\%$ Triton X-100. However, the existence of rafts in vivo is still under heavy discussion. Other alternative forces for membrane domain formation are discussed.

In general, the microdomains are too dense to be examined by confocal fluorescence microscopy and images show only slightly patterned distributions across the plasma membrane. Therefore most of the microdomain studies use indirect methods [13]. For instance, single proteins can be labeled by gold beads or fluorescent particles and the movement observed by a fluorescence microscope. Other methods analyze the fluorescence fluctuations within a spot of the plasma membrane or the fluorescence recovery after photobleaching to determine the diffusion constant of the lipid.

It is reckoned that STED might be the appropriate technique to investigate membrane microdomain distribution directly and with nanometer resolution. The first experiments are presented here. The proteins studied are involved in fusion of synaptic vesicles with the plasma membrane. The proteins' microdomains are enriched in cholesterol but not associated to the raft marker protein Thy1 [48]. In the first part of this chapter high resolution STED images of the microdomains are presented. Since the variation in density

between cells was very large, many images had to be recorded for a quantitative analysis. To facilitate the evaluation of brightness and density from a large number of images, FIDA (Fluorescence Intensity Distribution Analysis), a fluctuation method, was adapted to evaluate images of point-like objects. An introduction and proof is given in the second part. Last but not least, it is shown that the microdomains are very stable and are formed even on high overexpression of the protein.

### 3.1.1 Microdomains of fusion proteins imaged by STED

Exocytosis is a ubiquitous process occurring in eukaryotic cells. It is defined as the fusion of an intracellular trafficing vesicle with the plasma membrane. One of the protein families involved in exocytosis are the so called SNARE-proteins. (soluble N-ethylmaleimide-sensitive factor attachment protein receptors). Some of the SNARE proteins are associated with the vesicle membrane and others with the plasma membrane. Upon contact, the SNAREs are thought to assemble into complexes and pull the membranes very closely together what finally leads to fusion [49, 50]. This study focuses on the membrane associated neuronal SNARE-proteins syntaxin 1A and SNAP-25 which are keyplayers in fusion of synaptic vesicles with the plama membrane leading to neurotransmitter release (Fig. 3.2).

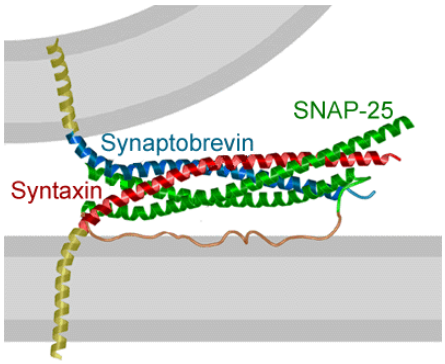


**Figure 3.2:** Synaptic fusion complex formed out of three different SNARE proteins: Syntaxin and SNAP-25 are attached to the plasma membrane and Synaptobrevin to the vesicle membrane. Modified from [51].

It was reported by fluorescence microscopy that syntaxin 1A is concentrated in 200 nm large cholesterol dependent microdomains representing specialized sites for fusion [48]. However, a quantitative description and analysis of such structures has been difficult due to technical limitations: Most of the microdomains imaged with a diffraction limited microscope where affiliated and did not allow proper measurements of the microdomains size. Now, the protein distribution was recorded with the three-fold increased resolution available with the STED microscope. The following images show that the resolution is sufficient to separate the clusters and quantitatively analyze the size and density of the spots.

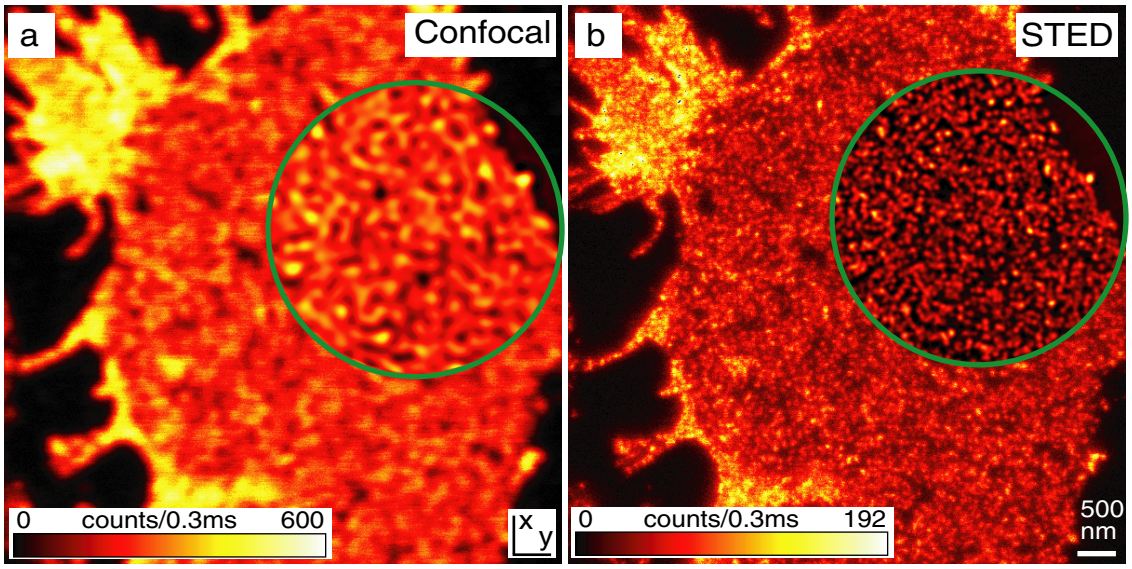


**Figure 3.3:** Immunostaing of SNAP-25 microdomains imaged by sub-diffraction microscopy. Raw data. a) Undulating intensity pattern in confocal mode while b) STED reveals distinct microdomains without background. inset: linear deconvolution of the corresponding area.

### Sample preparation[1]

In the past the membrane sheet preparation has been used to investigate SNARE proteins [48, 52, 53]. Cultured cells are subject to a brief ultrasonic pulse which disrupts the cell and only leaves the plasma membrane attached to the coverslip [54]. For a short period of time this membrane sheet is still functional. The advantage of this preparation is that the SNARE proteins, localized on the cytosolic part of the plasma membrane, are easily accessible by antibodies. Second, the images are almost free of background as there is fluorescence coming from the focal plane only and there are no cell components left which could be autofluorescent. All membrane sheets presented here were prepared from PC12 cells, a neurosecretory cell line, which are a model system for neuronal exocytosis. The membrane sheets were fixed with 4% paraformaldehyde, incubated with a syntaxin 1-specific monoclonal antibody, and subsequently labeled with a secondary antibody marked with Atto532. The coverslip was then mounted on a microscope slide with Mowiol. For details see Appendix A.1, [48].

### Imaging

The samples were imaged with a resolution of 65 nm in both (x and y) lateral dimensions determined using single primary antibodies visualized by secondary antibody as fluorescent point sources. The confocal and STED images were recorded in parallel, every line was recorded alternating once in the confocal mode (excitation light on) and once in the STED mode (excitation and STED light on).

[1] Sample preparation by Jochen Sieber and Thorsten Lang, Department of Neurobiology

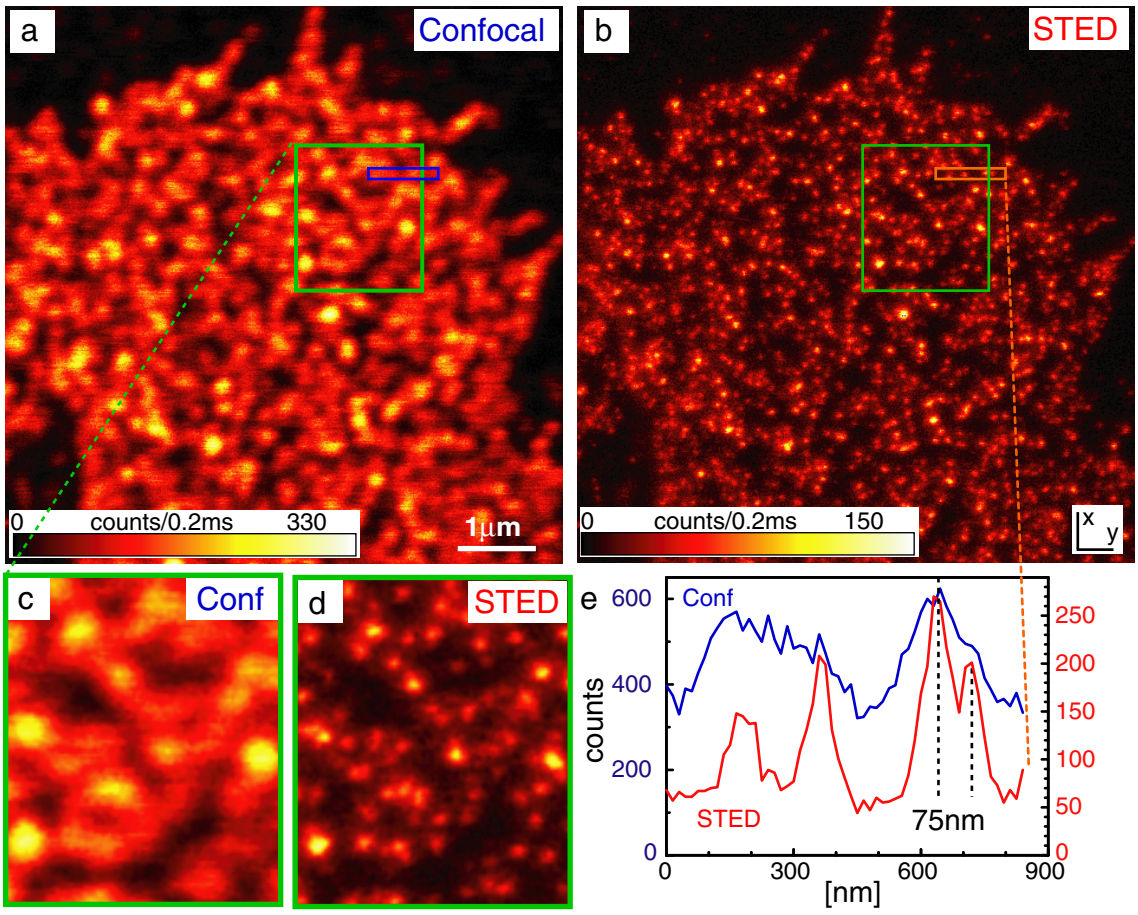


**Figure 3.4:** Syntaxin 1a microdomains imaged by STED microscopy. a) Confocal blurred image and b) separated clusters in the STED image. c) and d) The magnification shows well separated clusters only with STED. d) vertical sum of 4 lines. STED resolves clusters in a distance of 75 nm which is well below the diffraction limit.

Fig. 3.3 shows a SNAP-25 staining of a membrane sheet. While the confocal image shows a slightly patterned image, STED reveals the single dots with a good contrast. There is no underlying homogeneous background. The inset shows a linear deconvolution of the corresponding area. Negative values with an absolute value of 15% of the maximum intensity were accepted and replaced by zero. The PSF used for deconvolution was obtained by single antibody imaging, shown in Fig. 3.1. The average intensity of the excitation in focus was 1.3 $\mu$W and 15 mW of STED power.

In addition, the distribution of the SNARE syntaxin 1 was imaged. Fig. 3.4 shows a) the confocal and b) the STED image. Only the STED image separates most of the clusters whereas the confocal image shows blurred and overlapping dots. The clusters are less dense than SNAP-25 clusters and very homogeneous in brightness. The magnification in c) and d) shows that STED uncovers single clusters while the confocal image can not identify the same substructure. The clusters in the STED image are bright and clearly

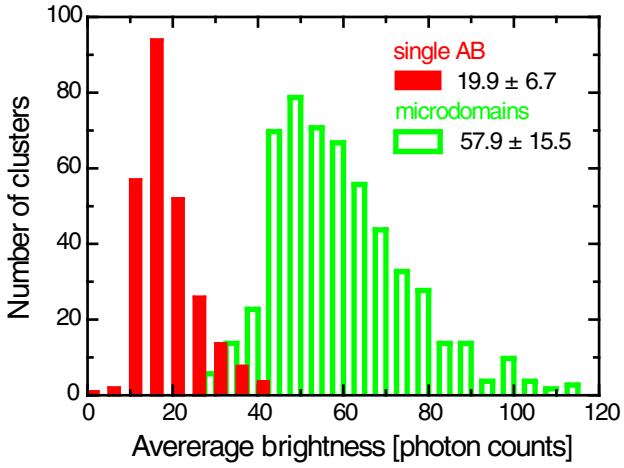


**Figure 3.5:** Brightness per pixel of single antibodies and syntaxin microdomains as denoted in the figure. Syntaxin clusters are about 3 times brighter. The values are average ± standard deviation

separated. The number of spots counted in the confocal and STED images reveal about three times more clusters per unit area than the confocal image (data not shown). Fig. 3.4.e shows a vertical sum of four lines as denoted in the image. Clusters of a sub-diffraction distance of 75 nm can be easily resolved. For this acquisition, an average excitation power of 1.9 $\mu$W and STED power of 17 mW in focus was used. Both images (Figs. 3.3 and 3.4) were recorded with a pixel size of 15×15 nm. Both images were excited at 470 nm. STED was applied at 615 nm. The fluorescence was detected between 525 nm and 575 nm.

### Results

Obviously, both examples, the syntaxin as well as the SNAP-25 microdomains could be better resolved in the STED image. All the signal is concentrated in defined spots of varying brightness indicating that all proteins are forming clusters. No homogeneous background is present which would indicate the presence of randomly distributed syntaxin or SNAP-25 protein. To distinguish clusters of protein from free unbound antibodies and to estimate the clusters size, it was necessary to show that every spot consists of more than one primary antibody. Therefore a sample of primary-secondary antibody agglomerates spread on a cover glass was prepared (compare Fig. 3.1, for preparation Appendix A.1) and imaged in the same way with the same laser power as the membrane sheets. Fig. 3.5 shows a histogram of brightnesses of single antibodies and syntaxin microdomains. The brightness is an average of all pixels within the FWHM of a cluster. Due to the fact that the mean of the brightness of microdomains is about three times higher than the brightness of single antibodies and the distributions are clearly separated, it is assumed that real syntaxin clusters were imaged and not unspecifically bound antibodies.

To conclude, single microdomains can be resolved. But how much information can be extracted of these images? Can the size of the clusters be determined which was pro-

posed to be 200 nm in diameter [48]? For an accurate size determination, the staining with three antibodies per cluster is not appropriate. Moreover, the syntaxin spots in Fig. 3.4 are only slightly bigger than single antibodies (Fig. 3.1) which indicates that the size of the microdomains is clearly smaller than the PSF of the microscope. To roughly estimate the size of the syntaxin clusters, 500 single spots were fitted by a Lorentzian. A spot size of $81 \pm 20$ nm was obtained. This corresponds to a cluster size of 48 nm in FWHM (assuming a PSF of 65 nm). It is important to mention that this refers to an average spatial distribution of the three antibodies. The antibodies, however, are spread randomly within the microdomains. Therefore the real size of the microdomain is larger than the value measured as the antibodies are most likely not only attached to the border of the microdomains.
For biological samples, additional information about the density (clusters per area) and brightness are essential to study the formation of microdomains under different conditions. Therefore it was necessary to find a method to evaluate whole membrane sheets instead of single clusters. The next chapter will introduce FIDA, which stands for fluorescence intensity distribution analysis, as a fast method to specify density and brightness of microdomains.

### 3.1.2 Microdomain ensemble analysis by methods of fluctuation spectroscopy

Being able to resolve most of the clusters separately, it was necessary to find an appropriate analysis method. To pursue biological studies, for example on syntaxin clustering in Chapter 3.1.3, detailed information of cluster density and the brightness of single clusters was required. Since the biological variation is typically very high, many images of different cells must be recorded and analyzed. A membrane patch contains up to a few thousand clusters and an evaluation of single clusters would be very time consuming. Moreover, the fact that not every cluster is clearly separated hampers a single cluster analysis. To speed up the evaluation, fluorescence intensity distribution analysis (FIDA) was adopted. FIDA is a statistical analysis techniques first described by Kask in 1999 [55]. FIDA and the more widely known fluorescence correlation spectroscopy (FCS) are commonly referred to as fluorescence fluctuation spectroscopy (FFS) techniques. These FFS technique usually rely on the detection of fluctuations in the fluorescence signal due to the diffusion of single molecules in solution in and out of the detection volume. Characteristics such as the length, the size or the density of these fluctuations can be used to obtain molecular parameters of the molecules under study, such as mass or size, fluorescence brightness or concentration. These molecular parameters can further render distinction of different species of a sample. In FIDA, the photon counts detected within time intervals of constant size are sorted into a photon counting histogram and are subsequent directly fitted. Such a fit necessitates a theory which expresses the probability of detecting a certain number of photon counts per time interval [56]. It seems obvious that this technique provides some information in imaging as well. Fluctuations in the fluorescence are obtained

in the same way, regardless whether the focal spot is scanned across the immobilized molecule, both enabling the determination of molecular parameters [57]. For FCS there is already an equivalent for analyzing images called image correlation spectroscopy (ICS) [58]. While in FCS the time trace of fluorescence fluctuations is correlated resulting in the molecules average diffusion time through the focus and its concentration, in ICS the two-dimensional (2-D) autocorrelation of images provides the average size and concentration.

A short summary of FIDA and ICS theory is presented. Thereafter these methods are used to evaluate membrane microdomain images. For a second control, the result of the evaluation is checked by single cluster analysis.

### Theory of FIDA

In the following a brief summary of basic assumptions of FIDA as introduced by Kask in 1999 [55] is presented. Further details can be found in [56].
First, a spatial brightness function $B(\mathbf{r})$is defined to account for the inhomogeneous focal spot, which is in general the effective PSF. The exact shape of the brightness function $B(\mathbf{r})$ is disregarded at the beginning. It is assumed that the observation volume is divided into a number of spatial sections with sizes $\Delta V_i$, each having an approximately constant value of spatial brightness, $B_i$. Using Poisson statistics, the probability of detection of $n$ photon counts from the volume element $\Delta V_i$ is expressed as:

$$P_i(n) = \sum_{m=0}^{\infty} P(m)P(n \mid m) \tag{3.1}$$

where $P(m)$ is the Poisson distribution of the number of molecules m in the volume element, and $P(n \mid m)$ the conditional distribution of the number of photon counts emitted by $m$ molecules. The mean value of $m$ is given by $c\Delta V_i$, where $c$ is the particle concentration. The mean of $P(n \mid m)$ is a function of the brightness $B_i$ and the time interval $T$: $mqB_iT$. Therefore the double Poisson distribution $P_i(n)$ can be expressed as:

$$P_i(n) = \sum_{m=0}^{\infty} \frac{(c\Delta V_i)^m}{m!} e^{-c\Delta V_i} \frac{(-mqB_i\Delta t)^n}{n!} e^{mqB_i\Delta t} \tag{3.2}$$

Now, the probability $P(n)$ of detecting n photons from the whole detection volume $V$ has to be constructed out of the probability $P_i(n)$ for a subvolume $\Delta V_i$. At first, it is assumed that $V$ is composed of only two subvolumes $\Delta V_1$ and $\Delta V_2$. The detected photons may be distributed arbitrarily among the two subvolumes while the sum has to be constant, yielding a convolution of the two probabilities:

$$P(n) = \sum_{i_1} P_1(i_1)P_2(n - i_1) = P_1 \odot P_2 \tag{3.3}$$

By splitting up the volume into $j$ subvolumes, a series of convolutions are obtained:

$$P(n) = \sum_{i_j} \prod_{j} P_j(i_j) \left( n - \sum_{l} i_l \right) = P_1 \odot P_2 \odot P_3 \odot \dots \tag{3.4}$$

The application of the theoretical function for fitting, which consists of a sum of convolutions is very time-consuming and thus unsuitable. The series of convolutions can be converted into a much simpler product by using the generating functions principle, a mathematical representation widely used in mathematical statistics. The generating function of $P_i(n)$ is defined by:

$$G_i(\xi) = \sum_{n=0}^{\infty} P_i(n)\xi^n \tag{3.5}$$

where $\xi$ is a complex number. If $\xi$ is restricted to the complex unit circle, i.e. $\xi \rightarrow e^{-i\varphi}$, then $G_i(\varphi)$ is the Fourier series of the probability distribution, and $P(n)$ can be reconstructed simply from $G(\varphi)$ by the inverse Fourier transform:

$$P(n) = \frac{1}{2\pi} \int G(\varphi) e^{-in\varphi} d\varphi \tag{3.6}$$

According to the convolution theorem, the series of convolutions of Eq. 3.4 can be converted into a product of its Fourier transforms:

$$G(\xi) = \prod_{0}^{\infty} G_i(\xi) \tag{3.7}$$

The derivation of the explicit expression for $G(\xi)$ is straightforward. First, the generating function of the double Poisson distribution of Eq. 3.2 is expressed using Eq. 3.5 and simplified by the serial expansion of exponential functions: $e^x = \sum_n x^n/n!$. Second, the generating function for the whole volume is obtained using Eq. 3.7. Finally, a Poissonian background with the mean value $\mu_{bg}$ was added to account for potential uncorrelated (background) signal and the summation over $\Delta V_i$ replaced by an integration over infinitesimal $dV$:

$$G(\xi) = exp\left( (\xi - 1)\mu_{bg}\Delta t + c \int_V \left[ e^{(\xi-1)q\Delta t B(\mathbf{r})} - 1 \right] dV \right) \tag{3.8}$$

The Fourier transformation of $G(\xi)$ results in the probability distribution $P(n)$, rendering the fit function used for describing the photon count number histogram of FIDA measurements. The brightness of the particle, $q$, and the density, $c$, serve as variable fit parameter.

The representation of the brightness function $B(\mathbf{r})$ remains. The authors of [59] found that a one dimensional integration, which is indeed much faster over the surfaces of constant brightness, is sufficient. Empirically they found a parametrization of the brightness profile in a confocal setup by:

$$\frac{dV}{du} \propto (1 + A_0 u + A_1 u^2) u^{A_2} \tag{3.9}$$

By setting $u \equiv -ln\frac{B(\mathbf{r})}{B(0)}$, a Gaussian profile would correspond to $A_0 = A_1 = 0$ and $A_2 = 0.5$. For a confocal setup these parameters are changed slightly to get good fit quality [56].

The effective PSF of a STED microscope is different from that of a confocal microscope. The profile is rather described by a Lorentzian than a Gaussian. To account for that, the volume parameters $A_0, A_1, A_2$ had to be adapted for the STED microscope to get best fit results. Applied to images, the resulting parameters of FIDA become the spot brightness as well as particle density.

### Theory of ICS

The power of fluorescence fluctuation analysis was realized with the implementation of fluorescence correlation spectroscopy (FCS) in 1974 by Elson and Magde [60]. FCS is a versatile technique that can provide the mean concentration of fluorescence particles and their diffusion constant. In as much as the diffusion constant of a molecule scales with its mass or size this information can be used to study reaction kinetics such as binding events in solution or in vivo. In image correlation spectroscopy (ICS), spatial fluctuations in microscope images are analyzed as opposed to temporal fluctuation in FCS. For FCS to be applicable, the temporal fluctuations in the samples must be small compared to the image acquisition time. Comparing ICS to FCS, the concentration of point-like objects corresponds to the particle concentration in FCS while the diffusion time corresponds to the average size of the scanned particles. ICS was first introduced as scanning fluorescence correlation spectroscopy for one dimension by Petersen [61] and was later on improved [62]. A good explanation including several examples is given in a review by Petersen [58].

The basic approach is a spatial autocorrelation $G(\xi, \eta)$ of an image with $i(x, y)$ being the intensity of the pixel at position $(x, y)$:

$$G(\xi, \eta) = \langle i(x, y)i(x + \xi, y + \eta)\rangle = i(x, y) \otimes i(x, y) \tag{3.10}$$

Where the angle brackets indicate spatial averaging. $\xi$ and $\eta$ are the spatial correlation lag variables. As the intensity $i(x, y)$ can be described as fluctuations $\delta i$ around the mean intensity $\langle i\rangle$, $i(x, y) = \langle i\rangle + \delta i$, $G$ turns out to be an autocorrelation of spatial fluorescence fluctuations,

$$G(\xi, \eta) = \langle \delta i(x, y)\delta(x + \xi, y + \eta)\rangle + \langle i(x, y)\rangle^2 \tag{3.11}$$

which can be normalized by the average pixel intensity $\langle i\rangle$

$$g(\xi, \eta) = \frac{G(\xi, \eta)}{\langle i(x, y)\rangle^2} - 1 = \frac{\langle \delta i(x, y)\delta i(x + \xi, y + \eta)\rangle}{\langle i(x, y)\rangle^2} \tag{3.12}$$

In the limit of $\xi, \eta \to 0$, $g(0, 0)$ gives the variance of the normalized intensity fluctuations. For non-interacting particles described by Poissonian statistics, the variance corresponds to the inverse of the average occupation number, $\bar{N}$ (density per beam area BA):

$$g(0, 0) = \lim_{\xi,\eta\to 0} g(\xi, \eta) = \frac{1}{\bar{N}} \tag{3.13}$$

The boundary value of $g(0,0)$ is used because of white noise present in every recorded image contributing to the central pixel.

The calculation of the autocorrelation can be facilitated by utilizing the convolution theorem. It states that the Fourier transform of an autocorrelation of a function corresponds to the product of the Fourier transform $\mathcal{F}$ of the function times the complex conjugate of the function's Fourier transform $\mathcal{F}^*$, i.e.

$$G(\xi,\eta) = \mathcal{F}^{-1}([\mathcal{F}(i(x,y))] \cdot [\mathcal{F}^*(i(x,y))]) \tag{3.14}$$

where $\mathcal{F}^{-1}$ is the inverse Fourier transform. These calculations were performed with standard 2-D fast Fourier transform (2D-FFT) system routines.

### Appraisal of FIDA and ICS results

It is very common in biological systems that a broad variation between cells of the same type and the same preparation is observed, even on one coverslip. Therefore, general results can be derived only on a large population of individuals. Thus, it is very important to rely only on biological results after averaging over many samples. In this section, the most probable bias of the fluctuation methods in use are considered.

Advantageously, the imaging of membrane sheets is almost free of background. All cellular parts which could cause autofluorescence were removed. As the sheet is very thin, there is no fluorescence originating from the parts out of the focus - assuming the sample is properly aligned. Further, it is obvious that the precision of the number density obtained by FIDA or ICS increases with the number of independent fluctuations, i.e. the image size. Here, the average size of the evaluated area was about $16\mu\text{m}^2$ with a focal beam area of about $0.013\,\mu\text{m}^2$. This is sufficiently large enough to gather enough statistical accuracy.

Regarding ICS, a proper function must be fitted to the correlation curve to determine the amplitude and the width. As the effective PSF in a STED microscope can be described by a Lorentzian, the correlation curve was fitted by a Lorentzian as well. It is more accurate to use a convolution of the Lorentzian PSF with a function describing the intensity profile of the domains to account for the expansion of the cluster. In an exemplary study, comparing both methods, the bias introduced by the simple Lorentzian fit was less than $10\%$ (data not shown). Thus, the evaluation was completly performed by the simpler Lorentzian fitting.

An average background of three photon counts per pixel was present due to counts of the employed avalanche photodiode, imperfect blocking of the bandpass filter, and due to some background fluorescence in the mounting medium. For the less dense membrane sheets, the average image intensity was only three times higher than the background. As the average image intensity is used for the normalization of $g(x,y)$ in Eq. 3.12, it must be corrected for the average background intensity $\langle i_{bg}\rangle$:

$$g(\xi,\eta) = \frac{\langle \delta i(x,y)\delta i(x+\xi,y+\eta)\rangle}{(\langle i\rangle - \langle i_{bg}\rangle)^2} \tag{3.15}$$

It was mentioned earlier that the white noise of the background only contributes to the zero lag amplitude of the correlation signal. It may be necessary to use a fitting routine

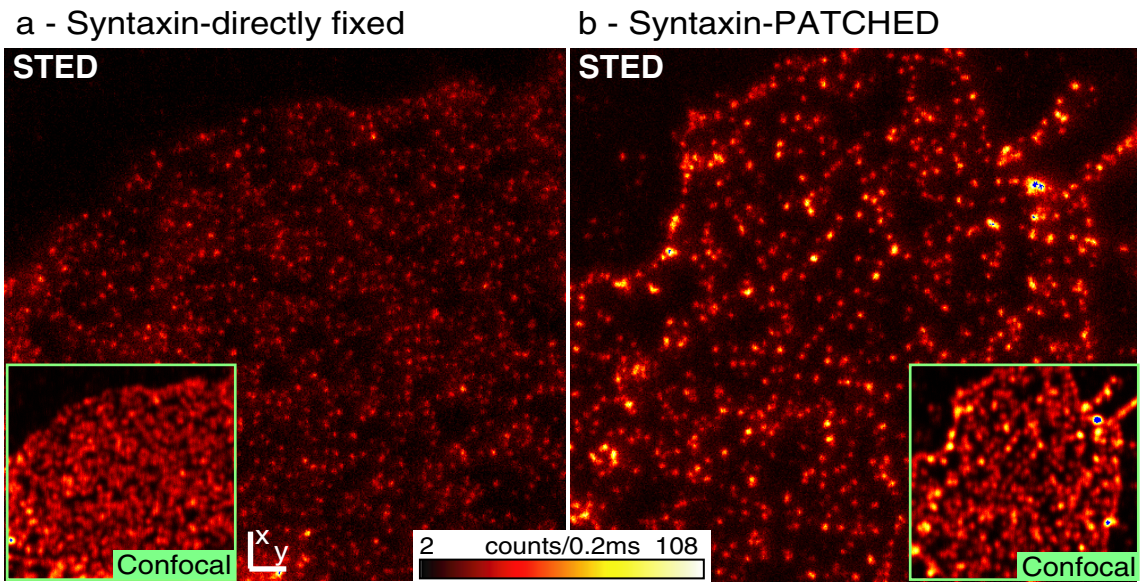


**Figure 3.6:** Syntaxin 1 on membrane sheets imaged by sub-diffraction STED microscopy. a) Directly fixed after disruption. b) Patching/aggregation of microdomains after 1h. The density is reduced resulting in larger and brighter clusters. The same color table and maximum value was used for both images. The confocal control of the respective STED image is shown in the inset.

where the $g(0,0)$ value receives zero weight. Here, the change in amplitude without weighting was less than $10\%$ and therefore neglected.

### Samples and imaging

The FFS methods are now tested with a large set of images of syntaxin microdomains as described in the first part of this chapter. To increase the variety of cluster density another technique was used to create artificially larger clusters. Some sheets where incubated before fixation in $200\mu\mathrm{l/CS}$ sonication buffer with $1\%$ BSA for 1h at $37°\mathrm{C}$ resulting in an aggregation or patching of plasmalemmal microdomains. Fig. 3.6 shows a) a membrane sheet immediately fixed right after removal of the cytosolic components while b) shows a membrane sheet incubated before fixation. The two pictures, which are representative of the whole set of data acquired, indicate the formation of syntaxin clusters: on one hand the density of the incubated membrane microdomains (PATCHED) is reduced and on the other hand the brightness of single microdomains is enhanced. Another significant effect can be seen in the PATCHED samples: the microdomains were sorted in a line on the edge of the membrane sheet. It is not clear why they moved to the edge but this was observed in most of the patched membrane sheets.

For image analysis, only those sheets were chosen which had a sufficient large size and no large, bright spots indicating remaining cytosolic or upper membrane parts. Apart from these criteria, the sheets were chosen randomly. Some images had to be sorted out later because the sheets were too small to be appropriate for fluctuation analysis.

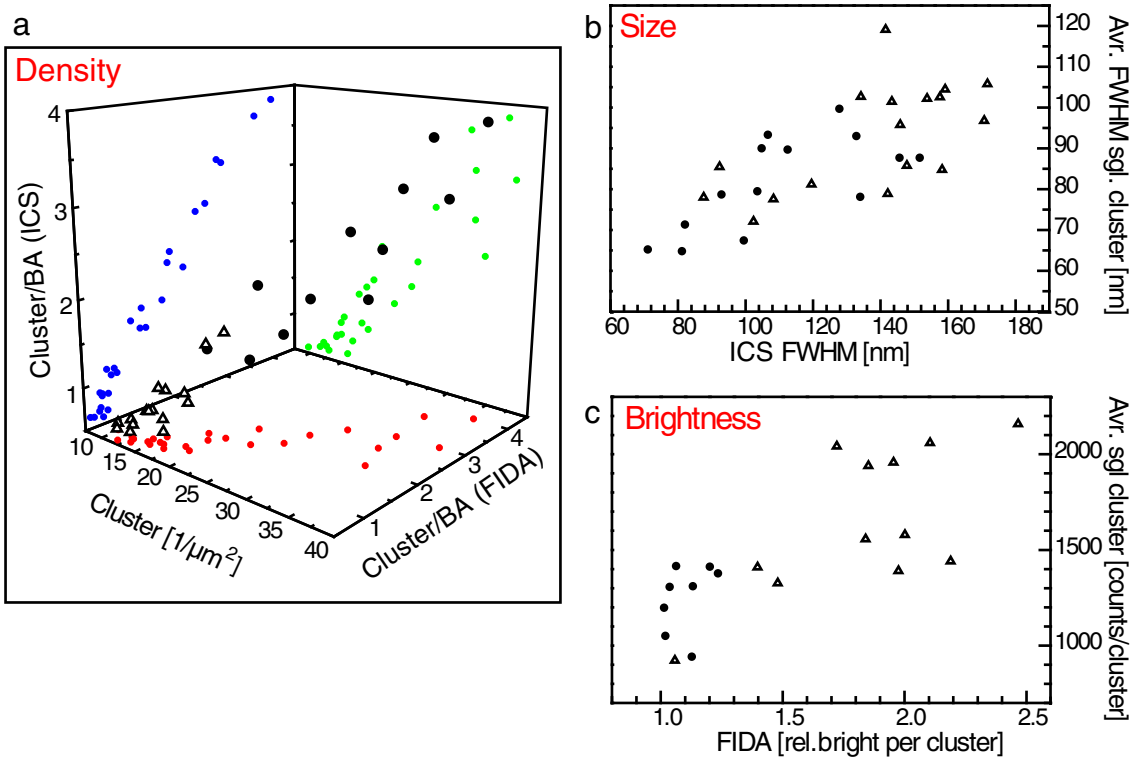


**Figure 3.7:** Comparison of the FFS techniques FIDA and ICS to a single clusters analysis. a) Three-dimensional representation of the cluster density. (● directly fixed membrane, △ patched membrane sheets) The projections to the 2-D planes are shown in color. b) and Cluster size and c) brightness evaluated by ICS and FIDA, respectively, compared to averaged interpretation by single cluster analysis.

For evaluation, the maximal rectangular area fitting completely into the membrane sheet was chosen and converted to a photon count histogram for the FIDA evaluation and the corresponding 2D-correlation data calculated for ICS.

### Results and discussion

Three kinds of information were obtained from image analysis: Density, brightness and size of the cluster in the membrane sheet. Analysis was performed by the FFS tools, FIDA and ICS, as well as by single cluster analysis. For FFS only relative values are obtained since each method uses slightly different definitions of the absolute values. Density is always referred to as probability per beam area, whereas the exact size and shape of the beam area is not known. Therefore, as a third method, not related to fluctuation detection, two kinds of software were used: one for the cluster counting and one for a fast evaluation of FWHM and brightness of single clusters[2]. For the FIDA evaluation a commercially available software (Evotec, Hamburg) was used.

[2]Software courtesy of Volker Westphal and Jan Keller, Department of NanoBiophotonics

It is difficult to realize single cluster analysis within an automated procedure as the cluster are aggregated by potential overlapping spots and variations in size and brightness. The algorithm used here is very simple. Starting at the brightest pixel, the program sums up all counts in the surrounding area of a user-defined radius. If the brightness is higher than a given threshold, it is subtracted from the image and counted as one cluster. This is repeated until every cluster is identified, i.e. no pixel brighter than the threshold is left. All images were evaluated with only small variations in threshold. A correction of the threshold was necessary only for high background or for very dark cluster.

The brightness and radius values resulting from the cluster analysis were determined with the help of a MatLab routine. The user interactively defined a region enclosing the fluorescent spot. The central lines were added up in the x- and y-direction (within the FWHM in y- or x-direction, respectively) and fitted by a Lorentzian, including a fit of the background. To rule out photobleaching, only the FWHM in x-direction, which was the fast scan axis, was regarded for size measurements. The brightness per pixel was defined as the sum of all photon counts within the FWHM in x- and y-direction.

Fig. 3.7.a shows a comparison of the results in density for all three methods: FIDA, ICS and single cluster analysis. Every pixel represents one membrane sheet. Each method is represented by one axis. If all methods correlated perfectly, meaning that they provide the same relative results, all points would be located on a straight line. It can be seen in the figure that the data indeed are correlated with some spreading due to the standard deviation of each method. The data points are projected to the XY, YZ and XZ planes showing correlation between two of the method. The best agreement is achieved for FIDA and ICS. This is not surprising, since both are based on the evaluation of fluorescence fluctuations. To count single clusters by eye or by software is a completely different task. Small variations of a few percent in the threshold can easily result in a 10-20% change in density.

In Fig. 3.7.b the average FWHM of single cluster fits is plotted versus the FWHM of the correlation curve in ICS. About 50-120 clusters per image were analyzed. It can be seen that the data are correlated with a standard deviation of about $30\%$. It was not possible to get a proper fit for every cluster in the single cluster analysis. Clusters residing too close together could not be accessed and others were big and frayed. To compare the result for the size by ICS with the single cluster evaluation, the same weighting must be applied. Due to the nature of the correlation function, each cluster contributes to the ICS analysis corresponding to the square of its brightness. Therefore, in the single cluster analysis the size $b$ of each cluster was weighted by its corresponding brightness, $q$: Average size of all clusters=$\sum q^2 * b / \sum q^2$. This means that the average weighted size corresponds to a sum over all clusters in an image whereas the cluster's size $b$ is multiplied by the square of its brightness $q$, for normalization divided by the sum over all brightness $q$ squared.

Fig. 3.7.c shows the correlation of average cluster brightness by single cluster evaluation to the brightness obtained by FIDA. Both methods correlate to some extent. In some images the brightness and density of the clusters was very homogeneous while in others a few big aggregates were present. But both fluctuation methods are based on Poisson distributed cluster intensities and one can not differentiate between these two assumptions.

| | Density [1/BA] from FIDA | Rel. brightness from FIDA | Size [nm] from ICS |
|---|---|---|---|
| Directly fixed | 2.40±0.84 (N=50) | 1.01±0.16 (N=50) | 114±25 (N=19) |
| Patched | 0.95±0.46 (N=50) | 2.28±0.97 (N=50) | 140±28 (N=24) |

**Table 3.1:** Comparison of directly fixed and patched membrane sheets, stained for syntaxin. Density values are per beam area (BA) and the brightness values were normalized for the direct fixed sheets. The size denotes the FWHM of the image correlation function (ICS). Values are average ± standard deviation. N is the number of analysed sheets.

On the other hand, FIDA would be able to identify two or three populations differing in brightness if such a model were a better fit to the photon count number histogram. Here, the patched clusters could not be described by two populations, although the patching could be regarded as fusion of two or more patches.

### Biological Significance

Previous data have shown that syntaxin cluster in freshly prepared membrane sheets have a defined size and distribution. When membrane sheets age, the SNARE reactivity decreases due to the formation of SNARE complexes within the native membrane [63]. The samples investigated in this study show a pronounced aging during the incubation at 37°C for 1 hour as indicated by the increase in cluster brightness and size (compare Fig. 3.6). In the following, the changes due to aging will be quantified. All data used for the correlation of the different methods in the previous section are summarized in Tab. 3.1 and averaged for the direct fixed and patched preparation. As expected, the density of the patched microdomains is reduced by a factor of 2.5, whereas the average brightness of the single cluster is increased. Both density and brightness were evaluated by FIDA. The brightness is a relative value, which was chosen to be about one for direct fixed samples. The increase in brightness is also reflected in an increase in size. The FWHM after ICS of patched microdomains was on average 1.3 times larger than the original directly fixed syntaxin cluster. To convert that value to an increase of the real size of the patch one has to take into account the following: From the FWHM of the autocorrelation function the average spot size can be calculated. Second, the spot size is a convolution of the object with the PSF, which results in a non-linear relation of the object's size and its spot FWHM (The increase in real size will therefore be larger than indicated by the increase in spot size). Third, the images represent the antibody distributions whereas the antibodies are randomly distributed within the patch (compare Section 3.1.1). A simulation of the antibody distribution on various patch sizes could provide real object size information.

To summarize, the results show that membrane aging is associated with an increase in size and decrease in density of syntaxin clusters. It can be concluded that membrane aging occurs rapidly after removal of cytosolic components and involves aggregation of plasmalemmal microdomains. This sheds new light on biochemical experiments that study plasma membrane microdomains on plasma membranes isolated upon lengthy fractionation procedures [63].

### 3.1.3 Syntaxin clustering by protein-protein interaction

In the plasma membrane, syntaxin clusters define sites at which secretory granules fuse. It is widely believed that lipid phases are mandatory for cluster formation, as cluster integrity depends on cholesterol. However, the native lipid environment is not sufficient for correct syntaxin 1 clustering. Additional cytoplasmic most likely protein-protein homospacific interactions are required [64]. Here, an indication for this hypothesis is presented: It is shown that the number of clusters directly depends on the syntaxin 1 concentration. An increase of the amount of syntaxin within the cells by overexpression did result in an increase in the density of clusters whereas the brightness and size of the clusters was not altered.

#### Introduction

For fast and efficient processing at the plasma membrane, for example of synaptic vesicle fusion, enrichment of required factors, as for example the synaptic fusion proteins syntaxin and SNAP-25, in specialized domains would be a postulate. It is therefore not surprising that protein inhomogeneities have been observed by different experimental approaches. They can be immunofluorescently labeled and visualized by microscopy. Biochemical experiments indirectly suggest the existence of microdomains as well. But the question remains as to what is the driving force for clustering. Detergent solubilization experiments led to the discovery of detergent resistent membranes (DRM), also called *rafts*, enriched in cholesterol, sphingomyelin and special proteins [65]. The raft hypothesis postulates that DRMs are stabilized by cholesterol and sphingomyelin and reflect microdomains in live cells. These lipids are supposed to form liquid ordered phases in the outer membrane leaflet, in which certain proteins preferentially participate via their GPI-anchor [47]. However, this does not necessarily mean that lipids alone are sufficient for membrane patterning.

In a collaboration with Jochen Sieber and Thorsten Lang[3], it was shown that protein-protein interaction could be a mechanism for fine tuning membrane patterns [64]. First, it was shown that no additional co-factors are needed because clusters form equally well in non-neuronal cells. Further by means of STED, it was demonstrated that the number of clusters directly depends on the syntaxin 1 concentration and therefore might not be limited by additional factors. Second, the cluster formation is highly specific: there is no mixing of syntaxin 1 with the very similar protein syntaxin 4 in the same cluster. Third, the SNARE-motif was identified to be required for cluster formation by protein-protein interaction. The SNARE-motif is a sequence of 60-70 amino acids, a homologue shared by every SNARE. In the case of syntaxin 1-4, this motif is anchored to the plasma membrane by a C-terminal transmembrane region (TMR), and attached to a large N-terminal domain via a linker region. For details of the biological motivation and results refer to [64].

[3]Department of Neurobiology, MPI for Biophysical Chemistry, Göttingen

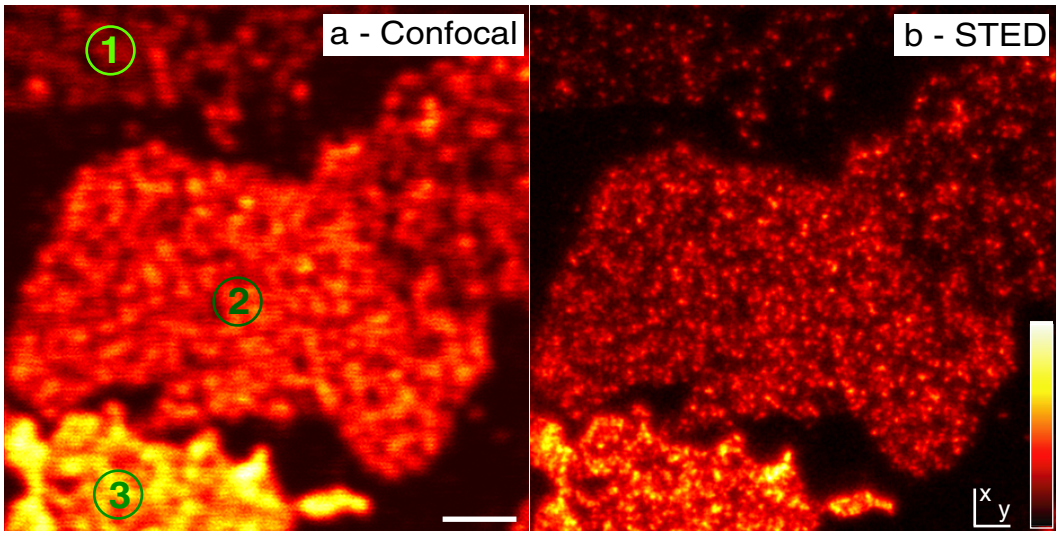


**Figure 3.8:** Syntaxin 1 labeled membrane patches at varying expression levels, whereas the signal intensity is regarded proportional to the syntaxin proteins in the membrane. Simultaneously recorded a) confocal image and b) STED image. Sheet (1) represents a low syntaxin density primarily due to endogenous proteins while in sheet (2) and (3) the syntaxin is medium and highly overexpressed, respectively.

In the following the contributing results obtained by STED microscopy are presented. After highly overexpression of syntaxin, only STED could resolve the clusters. The images were evaluated by FIDA and ICS as introduced in the previous section with regard to changes in cluster density, brightness and size as a function of the overexpression level.

### Results

To study the spatial distribution of overexpressed syntaxin 1, the same membrane sheets as in Section 3.1.1 was used: Neuroendocrine PC12 cells were disrupted by a short ultrasound pulse, leaving behind intact 2-D membrane sheets. The membrane sheets were immunostained for syntaxin 1A. For overexpression, the cells were transfected 48 hours before use. For details see Appendix A.1. Typically, about 30% of the cells were transfected and express additional syntaxin. Endogeneous as well as expressed syntaxin was labeled by the antibodies. Thus, density of syntaxin varies on a wide range as can be seen in Fig. 3.8. Sheet (1) is about the staining of lowest density, meaning that no syntaxin was expressed besides the endogeneous one. Sheets (2) and (3) of Fig. 3.8 show various levels of overexpression. However, most of the clusters could be separated without any obvious increase in background in the STED image but density increased linearly with image intensity (which is shown later). This is not possible with the confocal technique. If the syntaxin would depend on a putative co-factor, the distribution should become more unifom when elevated to levels largly exceeding endogeneous syntaxin, due to depletion of the co-factor. In the following, a closer look by a careful evaluation will reveal how

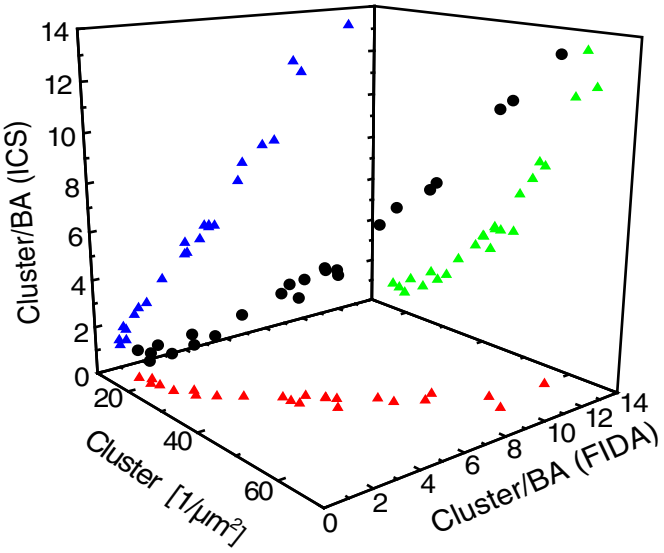


**Figure 3.9:** Comparison of three methods for density evaluation of overexpressed syntaxin 1A; number of cluster per $\mu m^2$ (Cluster $1/\mu m^2$) as determined by single cluster evaluation and number of clusters per beam area (BA) as detected by FCS and FIDA.

well clusters are formed at overexpression. For this , the FFS analysis tools FIDA and ICS were once again applied.

At first, the fidelity of the FIDA and ICS results was tested by single cluster evaluation. Fig. 3.9 shows a very good agreement of cluster concentration determined by FIDA and ICS. The data points are almost perfectly on a straight line. For high concentrations, the fluctuation methods yield slightly higher values of cluster density than the single cluster evaluation. This is probably due to the fact that at some point of density the clusters cannot be separated properly by the automated cluster evaluation algorithm, while the fluctuations are still detected by FCS and FIDA.

The issue of the relation between the cluster density and expression level still remains. It is assumed that the number of syntaxin in the cell is proportional to the intensity of the image. This should be a good approximation as they are sorted to a two-dimensional plane where they are always accessible by the antibodies. In Fig. 3.10.a, the density of 24 membrane sheets at different expression levels is plotted against the average image intensity and reveals a good correlation. Synatxin was increased up to 4-5 fold over endogeneous level (using a reference staining on membrane sheets from untransfected cells). In contrast, the size (Fig. 3.10.b) and average brightness (Fig. 3.10.c) of single clusters was not correlated to the image intensity. It should be noted that the highest overexpressions were even not resolvable by STED and therefore were not evaluated.

Summarizing, there was no difference in the structure observable upon high overexpresson. Although syntaxin is very abundant in the membrane, it can be increased dramati-

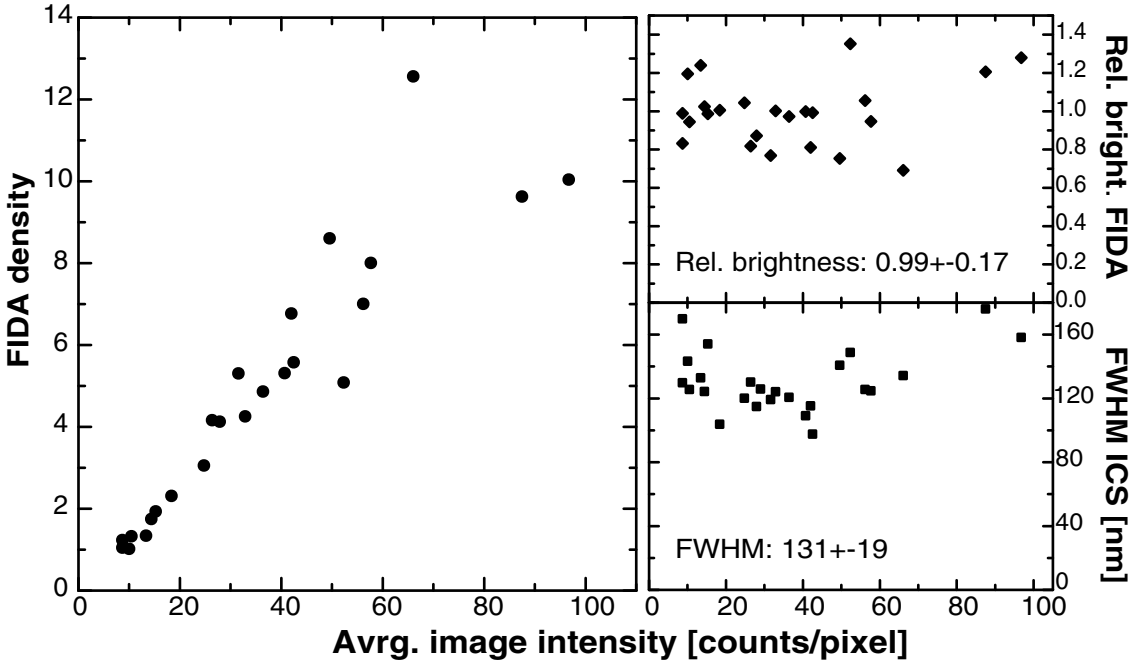


**Figure 3.10:** Correlation of density, brightness (detected by FIDA) and size (detected by ICS) with average image intensity. The total amount of syntaxin expressed is assumed to be proportional to the average intensity of the image. a) Linear increase of density with average image brightness, i.e. total amount of syntaxin. b) Cluster brightness and c) cluster size is not altered for higher expression levels.

cally with all syntaxin 1 still appearing in clusters. This might imply that no additional co-factors, apart from perhaps lipids, are essential for the clustering process.

## 3.2 Synaptic vesicles before and after fusion

Synapses are specialized junctions through which cells of the nervous system signal to one another and to non-neuronal cells. The transmission is mediated by neurotransmitters that are stored in synaptic vesicles and released by exocytosis upon activation. The vesicle membrane is then retrieved by endocytosis, and synaptic vesicles are regenerated and re-filled with neurotransmitter [66]. While many aspects of vesicle recycling are well understood, the fate of vesicle membranes after fusion is still unclear. Do their components diffuse on the plasma membrane, or do they remain together? This question has hitherto been difficult to answer because synaptic vesicles are too small (diameter $\approx$40 nm) to be resolved by epi- or confocal fluorescence microscopes, because of their diffraction-limited resolution of larger than 200 nm. Using the reduced focal area of the STED microscope, it was possible to visualize individual synaptic vesicles in the synapse by light microscopy. It is shown that synaptotagmin 1, a protein resident in the vesicle membrane, remains clustered in isolated patches on the presynaptic plasma membrane regardless, of whether the nerve terminals are mildly active or intensely stimulated.[4] It can be concluded that at least some vesicle constituents remain together during recycling. This is a further example of a study which documents that questions involving cellular structures with dimensions of a few tens of nanometers can indeed be resolved with conventional optics and visible light.

### Introduction

Synaptic vesicle recycling has been studied for more than three decades [67, 68]. In the best documented model of neurotransmitter release, the synaptic vesicle membrane collapses into the plasma membrane [67], a phenomenon which is referred to as full fusion. Fusion is believed to involve mixing of membrane constituents, at least to some extent, as well as diffusion of the vesicle constituents. Accordingly, to regenerate vesicles, sorting of vesicle proteins must occur at the plasma membrane after the neurotransmitter release and/or in an endosomal intermediate inside the synapse. However, if vesicle proteins remain patched together after exocytosis, accurate retrieval would be achievable without elaborate sorting because the recycling machinery would just have to internalize the fused vesicle patch rather than to recruit proteins scattered across the plasma membrane. So far it has not been possible to differentiate between these alternatives. Light microscopy cannot resolve individual vesicles because they are densely packed and have intervesicle distances below the diffraction limited optical resolution. Electron microscopy, on the other hand, provides sufficient resolution but the required labeling efficiency has hitherto not been achievable.

[4] In collaboration with S. Rizzoli and R. Jahn, Department of Neurobiology, MPI for Biophysical Chemistry, Göttingen.

### Imaging

One of the synaptic vesicle proteins is synaptotagmin. Synaptotagmin is a transmembrane protein with an intravesicular (lumenal) domain and an extravesicular (cytosolic) domain. For imaging, vesicles in the live neuron were targeted by a monoclonal antibody directed against the lumenal domain of the synaptotagmin [69], as sketched in Fig. 3.11.a. Upon neuronal activity, a synaptic vesicles opens to the outside space (exocytosis), rendering its internal components accessible to the antibodies. These bind to the synaptotagmin molecules and are internalized when vesicles are retrieved (endocytosis) [70]. Thus only vesicles undergoing exocytosis during the incubation time were labeled. After fixation, the internalized vesicles were visualized by a secondary antibody which was marked by a fluorescent dye molecule and directed against the primary, internalized antibody. The samples were permeabilized after fixation for the secondary antibody to penetrate through the plasma membrane of the synapse and the vesicle membrane. For details of the treatment see Appendix A.2.1. This method allows one to label only a few vesicles of a bouton containing a few hundred vesicles. Fig. 3.11.b shows an epi-fluorescent overview image of primary cultured hippocampal neurons incubated with the antibody at 37°C for 3 minutes. The gain in resolution of the STED microscope becomes evident by comparing the confocal image (Fig. 3.11.c) and the STED image (Fig. 3.11.d), displaying typical images. Whereas the standard method does not show substructures below the level of individual boutons, STED resolves numerous dots within the terminals, thus discerning individual synaptic vesicles. The average power (wavelength) of the excitation and the STED beams at the sample was 2 $\mu$W (470 nm) and 14 mW (615 nm), respectively.

### Control Experiments

The control experiments for the staining of synaptobrevin are shown in Fig. 3.12. To differentiate the synaptotagmin pool remaining on the surface of the plasma membrane from that internalized by endocytosis, two different protocols were used. First, labeling was performed on ice and in the absence of $Ca^{2+}$, i.e. conditions under which no endocytosis occurs. Bright staining was observed (Fig. 3.12.a). Second, labeling was performed at 37°C to allow for uptake of primary antibodies. This results in antibody binding and therefore labeling of synaptotagmin proteins to both surface exposed and internalized vesicles. To selectively label only the internalized pool, the surface-bound antibodies were blocked with unlabeled secondary antibodies prior to adding dye-labeled ones. As expected, the staining intensity of blocked, non-permeabilized preparations was barely above background (Fig. 3.12.b). Conversely, strong labeling was observed after permeabilization showing that the internalized (unblocked) were rendered accessible to secondary antibody labeling (Fig. 3.12.c). To further ensure that in the absence of permeabilization there is no antibody access to internal epitopes, neurons were labeled with a monoclonal antibody specific for the cytoplasmic tail of synaptotagmin [71]. Labeling was only observed when cultures were permeabilized prior to antibody incubation (Fig. 3.12.e and f).

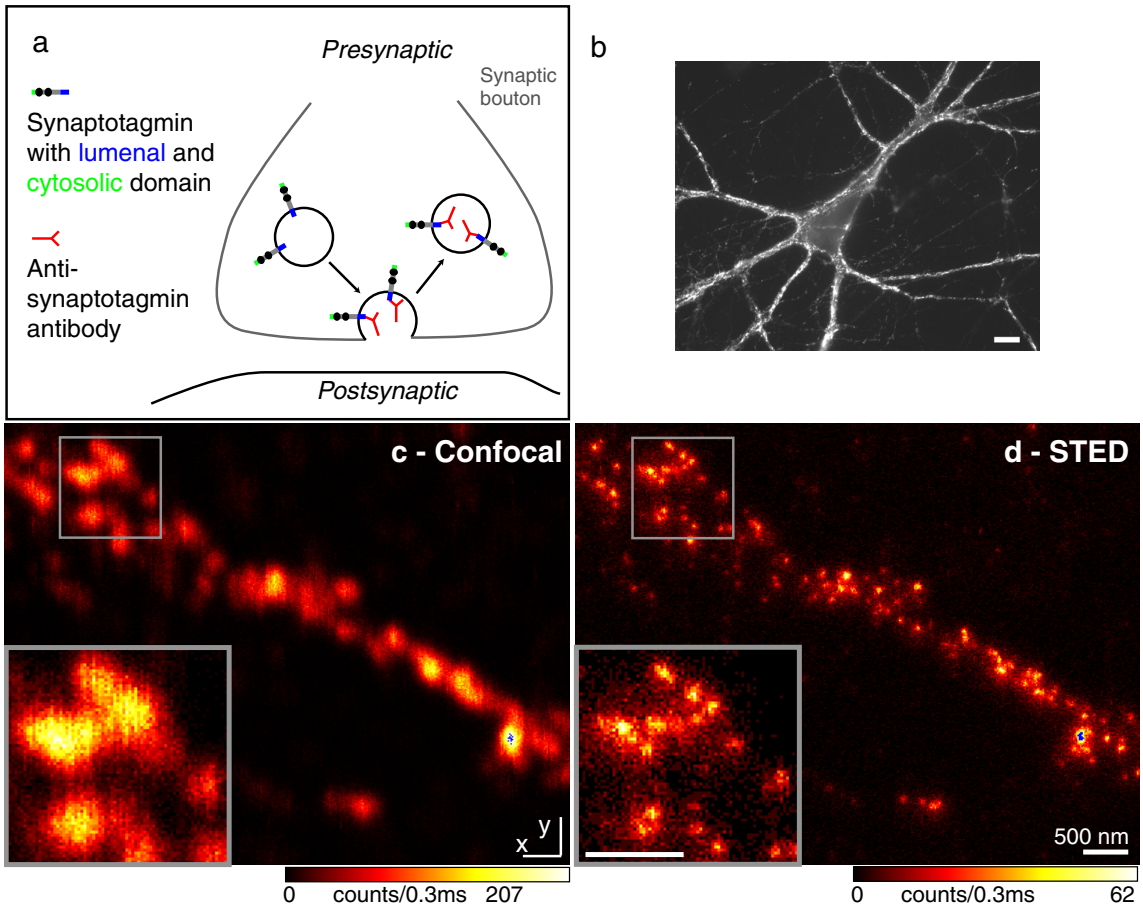


**Figure 3.11:** STED microscopy resolves synaptic vesicles of primary cultured hippocampal neurons. a) Mechanism of labeling: Synaptic vesicles exocytose and allow their lumenal synaptotagmin domains to bind anti-synaptotagmin antibodies; upon endocytosis the antibodies are internalized. b) Typical fluorescence wide field image of a neuron labeled with an anti-synaptotagmin antibody. Scale bar=10 $\mu$m. The same preparation was imaged by confocal (c) and STED (d) microscopy. The resolution is significant higher in the STED image.

## Results

Fig. 3.13.a and b show a comparison of surface-exposed and internalized synaptotagmin pools as resolved by STED-microscopy. Not only the internalized but also the surface-exposed pool was resolved into confined spots. Thus synaptotagmin remains concentrated in small clusters after exocytosis instead of being dispersed across the plasma membrane. The spots on the surface appeared to be brighter than those of the internalized pool. Therefore the spot brightness was quantified.
The spot brightness and FWHM were evaluated with a custom designed macro in MatLab. The user interactively defined a region enclosing the spot of fluorescence in the image. Background level and the FWHM of the focal spots in the x- and y- direction were de-

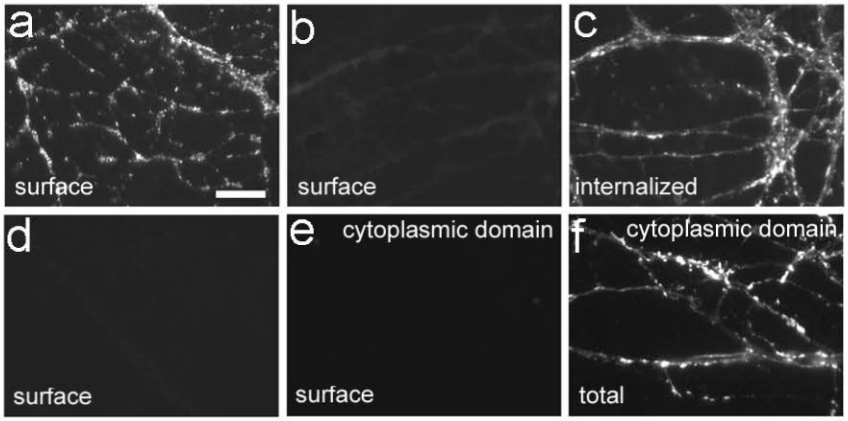


**Figure 3.12:** Control of the immunolabeling technique. a)-f) Wide field images of hippocampel neurons. a)-d) are labeled with antibodies specific for the lumenal (inside the vesicle) domain and e)-f) for the cytoplasmic (surface) domain of synaptotagmin. a) selective staining of the surface pool (low temperatur to prevent endocytosis) b) surface staining as in a) but secondary antibody was added after blocking the surface epitopes of the bound primary antibodies with unlabeled secondary antibody (negative control). c) selective staining of the internalized pool. d) cultures stained with secondary antibodies only (background control). e)+f) control, showing that an antibody specific for the cytoplasmic domain has no access to the cytoplasmic domain (e) unless the preparation is permeabilized after fixation (f). Scale bare=10 $\mu$m

rived from a Lorentzian fit to these spots. The brightness was defined as the background corrected sum over all pixels within the FWHM (compare Chapter 3.1.2).
For comparison, a dilute solution of primary antibodies was adsorbed on glass and labeled with secondary antibodies. The antibodies were imaged and quantitated parallel. The resulting histogram of spot brightness in Fig. 3.13.c shows (i) that both internalized and surface-exposed spots are significantly brighter than individual antibodies, confirming that each spot represents multiple synaptotagmin molecules. (ii) The brightness of the surface-exposed patches is shifted towards higher values when compared to the internalized vesicles. The latter is probably due to the brevity of the endocytotic process of 2-5 seconds [72], which limits epitope accessibility for the anti-synaptotagmin antibodies. Surface patches, on the other hand, were exposed to the antibody solution for a few minutes (on ice, to inhibit active recycling), resulting in a higher labeling efficiency.

But does the surface-pool of synaptotagmin remain clustered during high synaptic activity, i.e. under conditions when this pool is expected to undergo rapid turnover? To address this problem, the neurons were stimulated heavily with 70 mM KCl in presence of anti-synaptotagmin antibodies. Thereby the total surface fluorescence increased by more than two-fold (data not shown). However, the staining patterns of the surface pools (obtained from non-permeabilized preparations) were indistinguishable between stimulated and non-stimulated cultures (Fig. 3.14). Thus, even after massive exocytosis, synaptotagmin remains clustered in the plasma membrane.

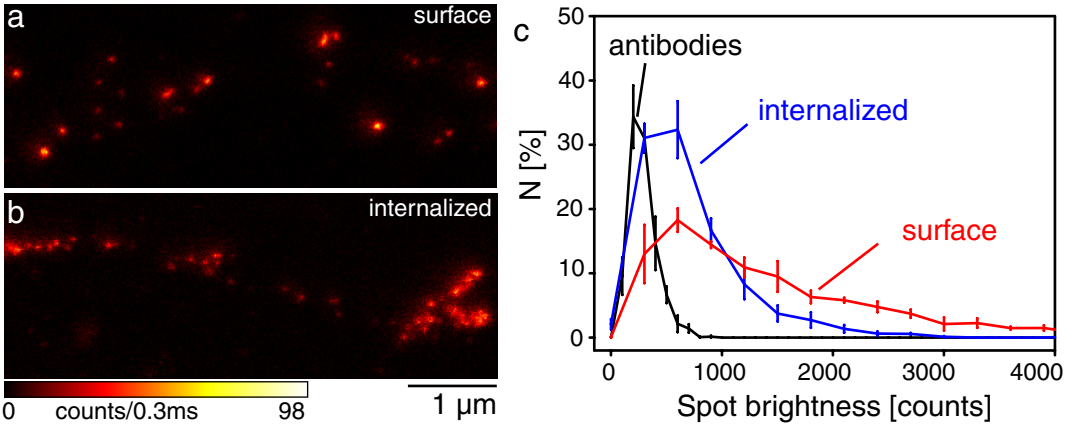


**Figure 3.13:** STED images. Comparison between surface-exposed and internalized pools of synaptotagmin shows that the protein remains clustered in the presynaptic plasma membrane. a) Typical STED image of surface-stained, non-permeabilized synapses. b) Typical STED image of internalized vesicles. c) Quantification of single spots, compared with the brightness derived from single antibodies adsorbed to glass. The histogram presents averages of 3-5 independent experiments. Note that the bin size is 100 units for the single antibody graph and 300 units for other curves.

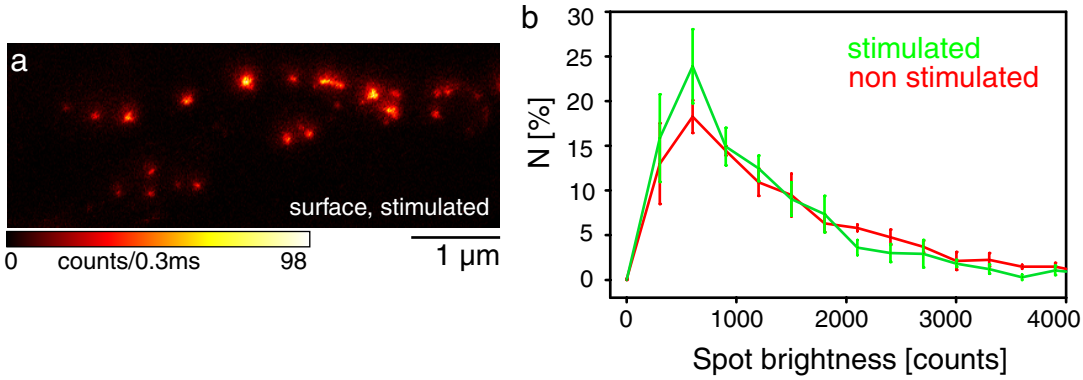


**Figure 3.14:** STED images. Spot sizes of surface-exposed synaptotagmin pools do not show major differences under stimulation. a) Typical STED image of a heavily stimulated, surface-stained preparation. b) Comparison of spot brightness of the surface pool in stimulated and non-stimulated preparations (mean ± SEM from 4-5 independent experiments).

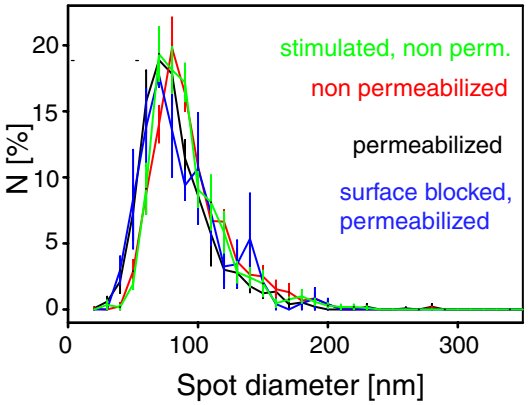


**Figure 3.15:** Quantification of spot FWHM for different preparations. Mean ± SEM from 3-5 independent experiments.

Finally, do the surface clusters represent the synaptotagmin inventory of individual vesicles or are they representing (at least in parts) aggregated patches? Therefore the diameter of the spots of the internalized pool was compared with that of the surface pool (Fig. 3.15). With all populations peaking at 70-85 nm diameter, no significant differences between the different populations are found. Considering 35 nm diameter as found by electron microscopy for synaptic vesicles [73] and the effective focal spot size of the STED-microscope (66 nm FWHM), a spot diameter of ≈70 nm is actually anticipated. This almost matches the peak in the measurement at 71 nm for the permeabilized preparation. (Fig. 3.15, number determined from log-normal fit to the histogram). A simulation of the patch size is more elaborate. A spherical 35 nm diameter vesicle results in a circular disc of 70 nm. While the vesicle membrane may spread out on 70 nm, it is the 2-5 labeled synaptotagmin molecules of the vesicle that is imaged and whose spatial distribution is of interest. These molecules can be modeled as virtually point-like objects of approx. 10 nm diameter (accounting for the size of the antibodies) that are randomly distributed within the 70 nm diameter patch. This model was used to simulate the STED-images of patches by convolving different constellations of synaptotagmin with the effective STED-PSF. The different constellations, including tilted orientation of the patch with regard to the optic axis, weighted according to the probability of occurrence, were considered. The peak of the simulated size distribution was at about 74 nm (Appendix Fig. A.1). This compares well with the about 81 nm found in the measurement for surface spots (Fig. 3.15, non-permeabilized). Thus, the observed values are in good agreement with the expected sizes.

## Discussion

In summary, it can be concluded that the synaptotagmin molecules of fused vesicles remain together as patches in the plasma membrane. Further, it is assumed that this behavior

is more or less paradigmatic for all protein vesicle constituents. These experiments also do not rule out the hypothesis that the protein components briefly disperse before being re-clustered. However, in view of the low number of single molecule intensity spots observed in these experiments, this situation is very unlikely.
It should be noted that previous observations suggested the dispersal of a vesicle protein (GFP-tagged synaptobrevin) out of the nerve terminals upon strong stimulation [74]. However, it remained uncertain whether the dispersal was caused by diffusion of patches or by the dispersal of individual molecules. Further, it is conceivable that overexpression of GFP-tagged synaptobrevin on top of the highly abundant endogeneous proteins results in an ”overflow” of molecules that cannot be retained in the vesicle protein cluster following exocytosis.
Finally, the first ever application of STED microscopy to a biological problem presents a major leap forward in the quantitative imaging of cells. So far, for analyzing details in the tens of nanometers scale, one had to resort to electron microscopy which is not always applicable. STED, on the other hand, provides an alternative solution while still maintaining the labeling efficiency of fluorescence microscopy along with its ease of operation.

## 3.3 Microtubules

Another application of an immunostaining (Atto532) is presented. Here the microtubular network of PTK (kidney from a rat kangaroo) cells are labeled (Appendix A.3). The cells were mounted with Mowiol (Appendix A.5) and imaged with the STED microscope. For demonstration, these samples were imaged with an effective PSF (Fig. 3.16.d) constricted only in one dimension instead of the previously used circular effective PSF which was constricted in two dimensions. This was obtained by a STED focal intensity distribution featuring two maxima (data not shown). For this purpose one half of the STED beam was phase retarded by $\pi$ as shown in Fig. 3.16.c. However, this effective PSF is sufficient to resolve single tubulin fibers as shown in Fig. 3.16.b. Hereby, the axis of subdiffraction resolution is oriented orthogonal to the direction of the fibers (i.e. horizontal). It can be seen in the image that the few fibers running horizontally are not subjected to increased resolution. A comparison of the confocal and STED image (Fig. 3.16.a and b) demonstrates once more that STED is capable of resolving relevant biological structures, whereas confocal is not.

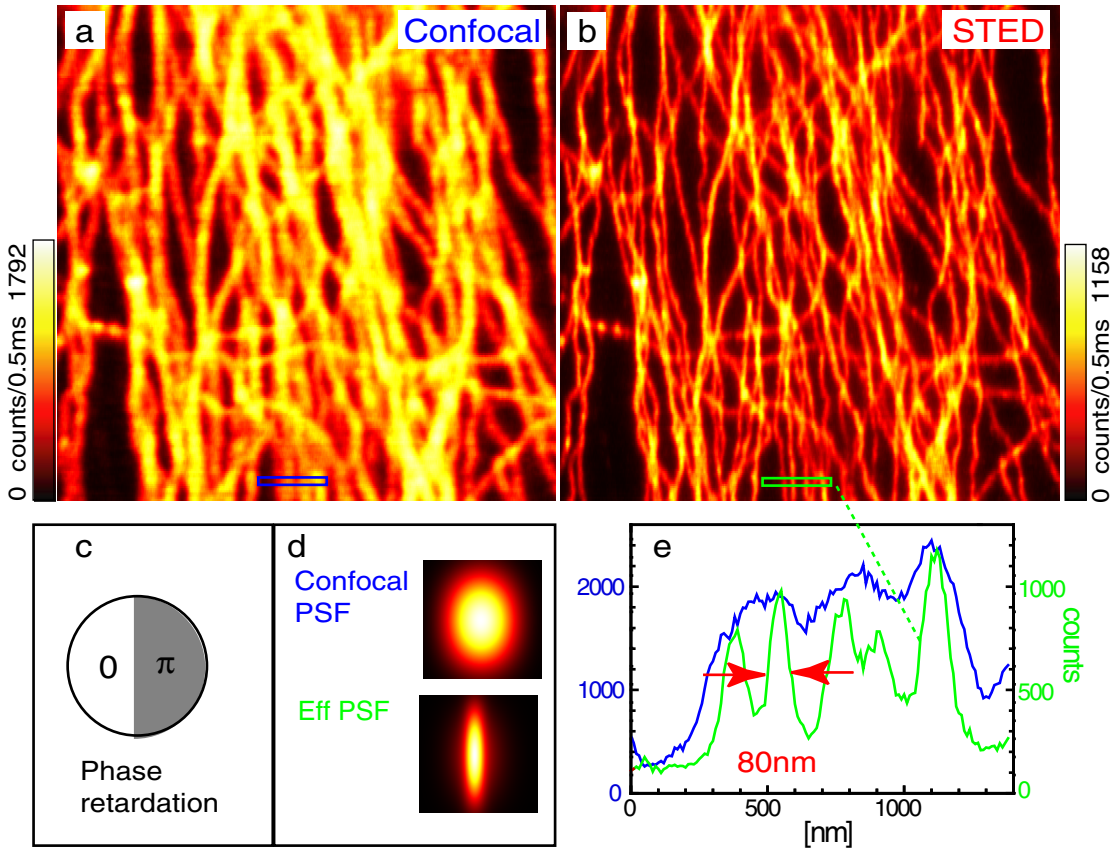


**Figure 3.16:** Tubulin fibers of a mammalian cell imaged by STED. The STED image (b) reveals most of the fibers separately whereas in the confocal image (a) most of the fibers cannot be distinguished. c) phase retardation implied by the SLM. d) Calculated confocal and effective PSF. e) Intensity profile (sum of two lines) as denoted in the images (a) and (b). The FWHM of the fibers imaged by STED is about 80 nm

# 3.4 Colloidal crystals

## Introduction

The term colloid (which from Greek meaning *glue*) stands for a two-phase system in which particles of one phase are dispersed in the other phase, for instance water, air or solids. The size of the dispersed phase particles ranges from 1 nm to 1 $\mu$m. There is often no particle sedimentation or phase separation because of their small size. On the other hand, the diffusion is very slow, emphasized by the term glue. Examples in every day life for colloidal systems are cosmetic products, milk, foam or smoke. Because of their size, they show characteristic behavior between the molecular world and the well known bulk properties. Since they are small particle, interactions between them play an important role, whereas they are generally not affected by quantum mechanics. Their large enough size to be visualized makes colloids a common model to study molecular behavior [75]. In water, most of the colloidal particles are characterized by a negative surface charge, meaning that there is a repulsive electrostatic force between them. Further, they are attracted by van-der-Waals forces. Therefore the effective potential can have a local minimum, which can result in binding of the particles analogue to the atomic binding [75]. For high volume fractions, these colloidal systems can crystallize into close packed structures. Depending on the speed of the crystallization process, the agglomeration can form disordered, amorphous structures or highly ordered crystals. As the diffusion of the colloidal particles is very slow, the crystallization process can be observed in reasonable times. In contrast, this would not be possible for the very fast crystallization of atomic crystals.

But what is the appropriate method to observe colloidal crystals ? Most of the structural information is obtained by either light or X-ray scattering. A limitation of these methods is that only information of the average structure can be extracted. No accurate information of local defects is possible. Preferable would be a direct observation of single particles in a microscope. An electron microscope would have the appropriate resolution but sample preparation is more difficult, it has to be dried or rapidly frozen [76]. Confocal fluorescence microscopy would be an attractive alternative: The sample preparation is easy, and beyond that dynamical processes can be observed. Unfortunately, the resolution here is much worse than in an electron microscope. The imaging of individual particles in concentrated colloidal dispersions by confocal scanning light microscope was first presented by van Blaaderen in 1993 [77, 76].

Recently, the same group presented the first ionic colloidal crystal of oppositely charged particles. By tuning the size and charge of the two particle species, they produced, for example cesium-chloride type and sodium-chloride type crystals [78]. Another example for an interesting study of crystal formation is an article published recently about melting of crystals [79] which showed a real time movie of the premelting starting at defects. Premelting is a localized loss of crystalline order at surfaces and defects at temperatures below the bulk melting transition. For this study particles of 750 nm diameter were used, limited by the resolution of the confocal light microscope.

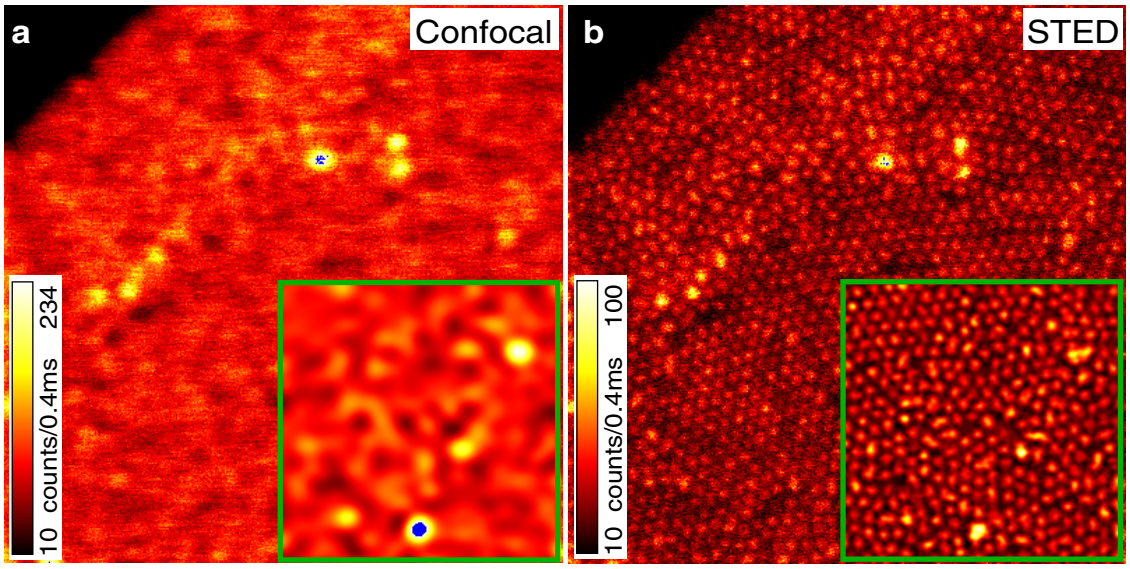


**Figure 3.17:** Single layer of colloidal particles. Compare cartoon in Fig. 3.18 for sizes. a) Confocal and b) simultaneously recorded STED image (raw data), which reveals every particle. Some parts show hexagonal ordering. Inset: linear deconvolution of corresponding area.

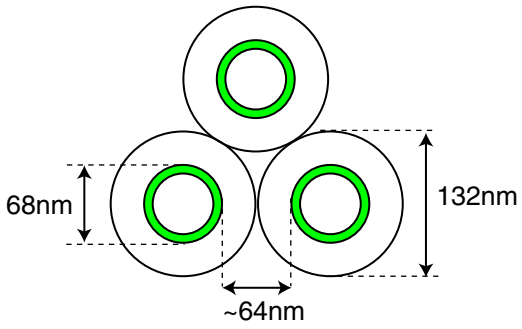


**Figure 3.18:** Colloidal particles with fluorescent inner shell

The ease of handling of a fluorescence microscope combined with a resolution of a few tens of nanometers can be provided by a STED microscope. The first STED images of silica spheres of 132 nm diameter labeled with the fluorescent dye Atto532 are shown. The study of colloidal crystals on a length scale which is more than 5 fold smaller than the previously studied colloids [79] is supposed to give rise to new insights into crystal formation.

## Imaging

Similar colloidal particles as used by the group of van Blaaderen were synthesized[5]. Using a chemical synthesis technique particles with a fluorescent core of 68 nm and a non-fluorescent shell of 132 nm diameter were produced. This is well below the diffraction

[5]Colloidal particle synthesis by Marianno Bossi, Department of NanoBiophotonics

limit of an optical microscope. The particle size, after every synthesis step, was determined by a transmission electron microscope (TEM). For details see Appendix A.4. By a technique consisting of slow evaporation of the solvent (ethanol) over the weekend, the spheres attached to a coverslip in a self-assembling manner [80]. The coverslip was then mounted on a microscope slide using immersion oil as mounting medium.

The microscope was running as previously described. With the STED beam forming a doughnut in the focal plane, the effective PSF was constricted in both lateral dimensions. Along the optical axis no confinement was applied. The effective PSF was therefore rather elongated by a ratio of 10:1 (axial:lateral). The superresolution of the STED microscope in the lateral plane was demonstrated on a monolayer of colloidal crystals, shown in Fig. 3.17. While the confocal image (a) shows only slight modulations, the spheres are well resolved in the STED image. The confocal image was recorded with 1.3 $\mu$W (470 nm) in the focal plane. The STED image was simultaneously recorded by turning on the STED beam of 14.0 mW average power (615 nm) in the focal plane. Only a few brighter spots in the image indicate that some one or two particles are on top of the layer at these positions. The contrast of the STED image can even be increased by a linear deconvolution as shown in the inset. Most of the particles shown are hexagonal ordered. The largest area of ordering encloses about 60 silica spheres. The upper left corner of the image shows a sharp border of the colloidal particle arrangement. Fig. 3.18 shows a cartoon of the colloidal particle arrangement. The distance of the center of two neighboring particles is at least 132 nm whereas their fluorescent shells are only about 64 nm apart.

These images demonstrate that STED is indeed capable of resolving colloidal particles closer together than the diffraction limit of light. Since a 5 fold decrease in diameter (compared to the particles of 750 nm diameter used previously [79]) results in a 25 fold reduction in surface and as the surface plays an important role in the particle interaction, a switch to a high resolution STED microscope has the ability to open up new insights in colloidal physics.

# 4 STED on the green fluorescent protein (GFP)

## 4.1 Introduction: GFP - a widely used biological marker

Since the discovery of the fluorescent proteins and cloning of their genes, they have been widely used as minimal invasive markers, appropriate also for live cells (see also Chapter 2.2.2). For staining, the gene of the fluorescent protein is fused in frame with the gene encoding the endogenous protein and transfected to the cell. The resulting chimera protein is expressed in the cell or organism of interest. The ideal result is a fusion protein that maintains the normal function and localization of the host protein but is now fluorescent [10]. Fluorescent proteins have been targeted successfully to practically every major organelle of the cell. Examples are the plasma membrane, mitochondria, Golgi apparatus, secretory vesicles, etc. . Thus the rather large size of the GFP and the differing pHs of such organelles do not seem to impose a barrier whereas the fluorescence of some GFP mutants can be very sensitive to pH. These mutants are used, for example, to report synaptic neurotransmitter secretion [45].
The combination of tagging live cells with fluorescent proteins and new fluorescent imaging methods allow to study kinetic behavior of various proteins. One of these new imaging techniques is fluorescence recovery after photobleaching (FRAP), in which an area of the cell is photobleached and the movement of unbleached molecules from the neighboring areas into the bleached area is recorded. Another example is fluorescence correlation spectroscopy (FCS). Here, by observing the molecules fluctuating through the focal volume, the protein's diffusion constant can be obtained [11].

Therefore the fluorescent proteins have opened up new possibilities in biology. The field of live cell imaging has emerged significantly. As the dye is produced by the cell itself, even organs of living animals can be stained by gene transfection. Without doubt, the use of fluorescent proteins in STED microscopy combines the finesse of biological staining with the superior resolution of STED.

## 4.2 GFP - a label for STED microscopy

Although GFP is a very stable protein and is very resistant to photodamage, would it be applicable for STED imaging? To address this issue a bright and simple sample, most

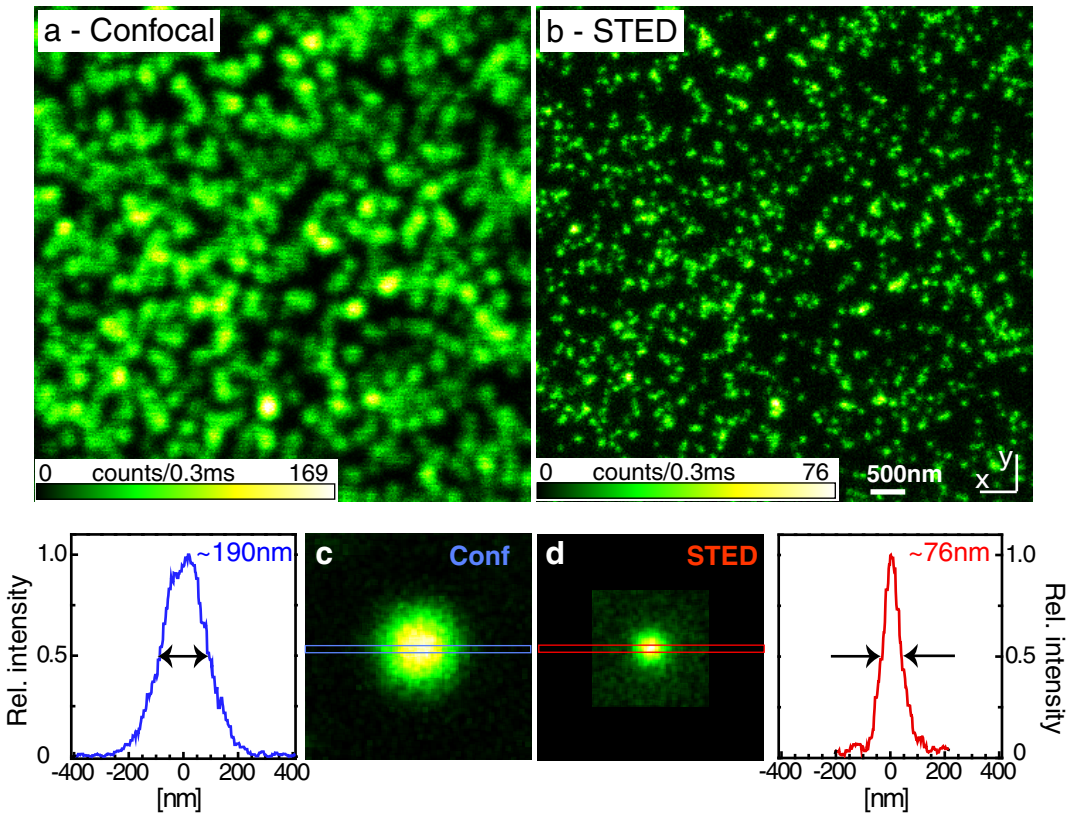


**Figure 4.1:** Virus like particles containing GFP a) Confocal image recorded with 488 nm excitation light and b) simultaneously recorded STED image by turning on the STED laser at 575 nm. c) and d): Overlay and profile of 10 confocal and 10 STED spots, respectively, obtained from a more diluted sample. The STED spot is about 2.5 times smaller in size. Note that the actual particle size is 40 nm in diameter (obtained by EM) leading to spot sizes broader than the FWHM of the effective PSF.

suitable with a known size of the structure, was needed. The perfect sample therefore was a virus-like particle (VLP) containing 120 GFP molecules, a kind gift from the laboratory of Jean Cohen, France [81]. The used virus was a rotavirus which is perfectly spherical and has a defined size. It consists of three concentric capsid layers. The innermost layer protein, VP2, was coupled to a GFP protein without altering the auto assembly properties of the virus. It was shown that every VP2 was substituted by a chimeric VP2-GFP and that at least 95% of the GFP domains were properly folded. There was no quenching detected even though the molecules were very close together. Since there are exactly 120 VP2 molecules forming this inner shell of the virus, the same number of GFP molecules are present in the virus. The diameter of the GFP shell is about 40 nm as determined by cryo-electron microscopy (cryo-EM) [81].

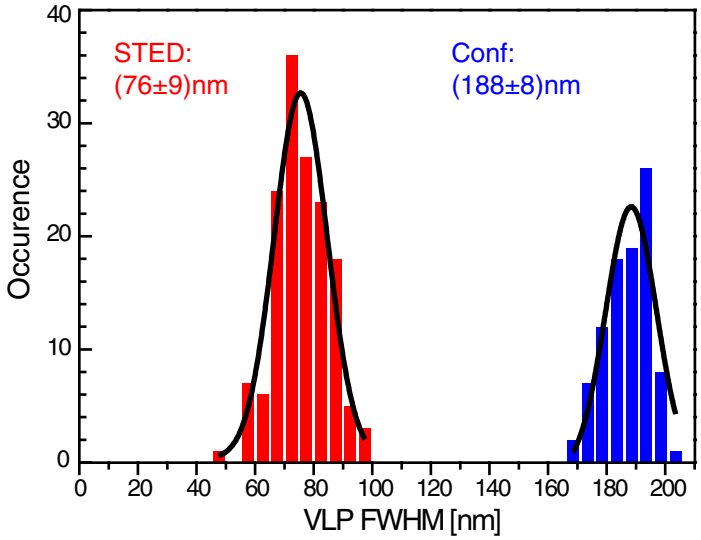


**Figure 4.2:** Size distribution of VLPs containing GFP. The distribution was fitted with a Gaussian fuction, revealing the mean sizes ± standard deviation as denoted in the figure. The mean spot size in the STED image is 2.5 times smaller than in the confocal counterpart.

### Imaging of VLP-GFP

The VLPs were fixed with 4% paraformaldehyd and diluted in PBS. A drop was spread on a coverslip. After evaporation of the solvent, the coverslip was mounted on a microscope slide with Mowiol (Appendix A.5) and imaged. Fig. 4.1 shows the confocal and STED image with an excitation of 0.07 $\mu$W average power in the focal plaine at a wavelength of 488 nm and 7.2 mW at 575 nm for STED. The pixel size in both images was 20 nm$\times$20 nm. Although the confocal image shows a blurred and rather branched structure the STED image reveals the point-like structure of the object. There are dark spots, small bright spots and brighter blobs. A careful analysis of images of a more diluted sample (not shown) illustrate that single VLPs are visible in the STED image. The occurance of dark and bright spots in Fig. 4.1 of the same size suggests that dark spots are single VLPs, whereas brighter spots are aggregated clusters of two or more VLPs. This was expected as the brightness distribution of a single VLP can only vary within the bias due to Poisson statistics of the detected photons; the total number of 120 molecules per VLP is constant. Due to the low signal of single VLPs 10 spots were averaged and are show for clarity (Fig. 4.1.c and d). These spots were chosen from a more diluted sample where the VLPs were clearly separated both in the confocal and in the STED image. The images of single spots were interpolated to a 10 times smaller pixel size and superposed by calculating the center of mass for each spot. As a result it could be shown that the spot size was dramatically reduced from a FWHM of 190 nm to 76 nm by STED.

### Resolution of the microscope

Since the size of single VLPs is known, the resolution of the microscope can be easily determined. First the FWHM of 150 spots from two different STED images and 93 spots from two confocal images of the same sample was measured. For this purpose a custom designed MatLab routine was used (compare Chapter 3.1.2). For each spot a surrounding rectangular area was interactively defined. Then a Lorentzian function was fitted to the horizontal sum of all lines which are within the FWHM of the vertical direction. The FWHM of the fitted Lorentzian was sorted to the histogram shown in Fig. 4.2. The average spot size of the STED image is 2.5 times smaller than the confocal control. However, this analysis is based on the spot size and is not exactly the resolution of the microscope. Since the spot size is a convolution of the object with the PSF and the size of the VLP was previously known to be 40 nm in diameter, the resolution can be estimated by a simulation. It should be noted that a deconvolution would be more inaccurate and would not reflect the real size of the PSF. It is assumed that the profile of the effective PSF of the STED microscope can be approximated by a Lorentzian function. Therefore two dimensional Lorentzian intensity distributions of different sizes (FWHM) were generated and convoluted with the the two dimensional intensity distribution of a particle of 40 nm diameter. The spot size of the convolution agreed with the the measured spot size of 76 nm for a Lorentzian PSF with a FWHM of 70 nm.

In conclusion, GFP stained samples can be imaged with a PSF of 70 nm FWHM in two dimensions. The following section will show first GFP stainings of biological interest.

## 4.3 Size distribution of Dnm1p-GFP, a mitochondrial fission protein in yeast

### Introduction

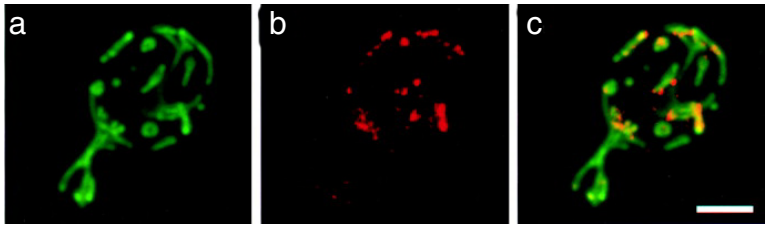


**Figure 4.3:** Dnm1p clusters are attached to yeast mitochondria. a) mitochondrial network b) Dnm1p staining. Both images are merged in c). Scale bar 2 $\mu$m. Adapted from [82].

Mitochondria are the power source of a cell. They are double membrane-bound organelles with highly specialized function and morphology. Mitochondria form dynamic tubular networks that continually change their shape and move throughout the cell. Moreover, they permanently undergo fission and fusion; two dynamically opposed processes.

These pathways rely on conserved GTPases, enzymes which can bind and hydrolyze GTP. Most of these processes were studied in the budding yeast *Saccheromyces cerevisiae* whereas most of the proteins are conserved in humans, mice, and plants [83].

Dnm1p, a dynamin-related GTPase, is one of the proteins involved in mitochondrial fission in yeast. Fig. 4.3 shows that Dnm1p can assemble into punctuate structures on mitochondria in living cells [82]. This figure shows in a) the typical branched structure of the mitochondrial network and in b) the spots of Dnm1 clusters. In a model of mitochondrial fission, the Dnm1p forms a ring around the mitochondrial tubule at a position, which was constricted previously by another unknown process. Recently it was shown by electron microscopy (EM) that purified Dnm1p formed *in vitro* rings by self-assembly with a diameter of 109 nm. This is well beyond the diffraction limit of a light microscope [84]. In the same study, mitochondrial constrictions were determined to be of the same size. Therefore Dnm1p spirals could be formed around the mitochondrial constriction and thus mediate fission. Nevertheless, a final conclusion can only be drawn if a ring would be visible in an organism. As it seems to be very unlikely that this can be achieved with EM, STED is the most favorable method. Unfortunately, most of the Dnm1p assembles in clusters and only about 1 out of 30 spots would represent a ring (private communication). Moreover, the ring would have to be oriented parallel to the image plane in order to be visible.

However, although ring like structures could not be identified, the following images of Dnm1p-GFP show the first STED images of a GFP staining. On a basis of 70 nm resolution, the size distribution of the Dnm1p clusters attached to the mitochondria was measured.

### Imaging of Dnm1p-GFP

Yeast cells with epitope tagged Dnm1p-GFP[1] were grown in Y-Gal media (yeast extract peptone-galactose media). The strain used in this study was isogenic to BY4741. The wildtyp *DNM1* gene was disrupted by the inserts of *DNM1*-GFP-loxP-kanMX-loxP cassette. The protein Dnm1p-GFP was still functional. The cells ware fixed with 4% paraformaldehyde, washed, and spread on a coverslip. After evaporation of the water they were mounted on a microscope slide with Mowiol (Appendix A.5) and imaged under the same conditions (especially with same excitation, STED power and pixel size) as the VLPs in the previous paragraph. Therefore the FWHM of the effective PSF of the STED microscope can be assumed to be 70 nm. Only yeast cells attached to the coverslip were image. Therefore penetration into the yeast/Mowiol was only a few $\mu$m, and a resolution loss due to aberrations can be neglected.

A lateral cross-section of a yeast cell, expressing Dnm1p-GFP, is shown in Fig. 4.4. The confocal as well as the STED image show a few bright and several dark spots. Only the bright spots were in the focal plane whereas dark spots are slightly above or below it. The border of the cell is outlined by a gray line. It was identified by a slightly larger

[1] Collaboration with Astrid Schauß, Department of NanoBiophotonics

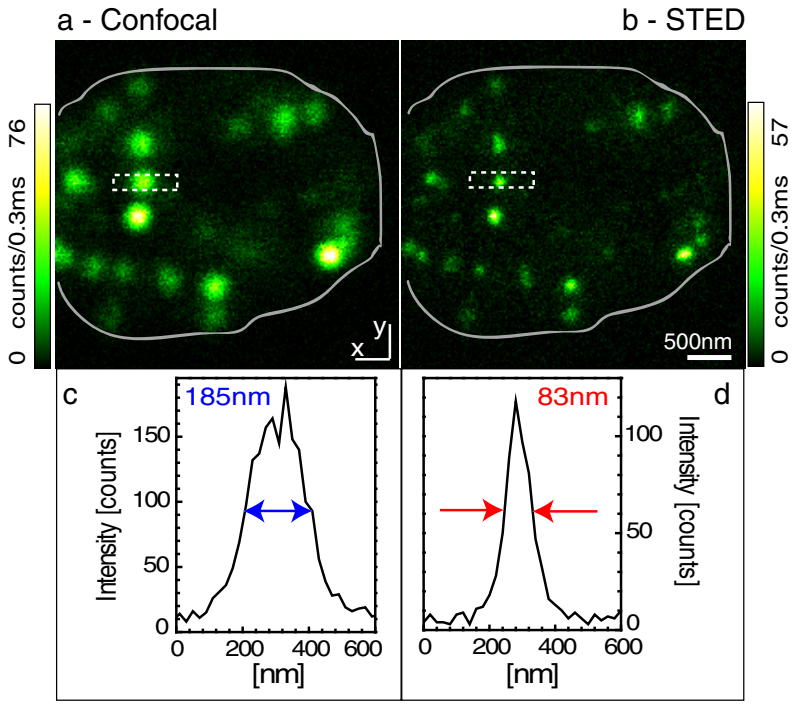


**Figure 4.4:** Lateral cross-section of a yeast cell expressing Dnm1p-GFP. a) Confocal versus b) STED image. The cell is outlined by a gray line as a guide to the eye. The confocal (c) and STED (d) profiles are the sum over the 4 central, horizontal lines of the spot marked in the image.

background intensity inside the cell. The image demonstrates that the size of the Dnm1p clusters is below the diffraction limit of the confocal microscope. The intensity profile of the cluster indicated in the image shows clearly a smaller FWHM of 83 nm with regard to the confocal counterpart of 185 nm. For a more precise measurement of the cluster size several images were recorded. The cluster analysis is shown in the following paragraph.

### Size distribution of Dnm1p-GFP clusters

Several images, similar to the one shown in Fig. 4.4, were recorded. Only those spots were taken into account where the intensity of the brightest pixel was above 25 counts. Accordingly only up to about three spots per cell were evaluated. Four central, horizontal (x-direction) lines were summed up for a better signal to noise ratio of the profile. Then, the width of the profile was measured at about half of the maximal intensity. As the error of the size measurement was about 2 nm, a more time consuming fitting was not necessary because the error is well below the error expected for variations in biological samples. Fig. 4.5 presents the size distribution of 94 spots with a mean of 114 nm. This diameter of 114 nm, a value below the diffraction limit, is in disagreement with a previously published value of 300-400 nm [85] which is probably due to their microscope of limited resolution. The standard deviation, representing the width of the distribution, is 21 nm, which is

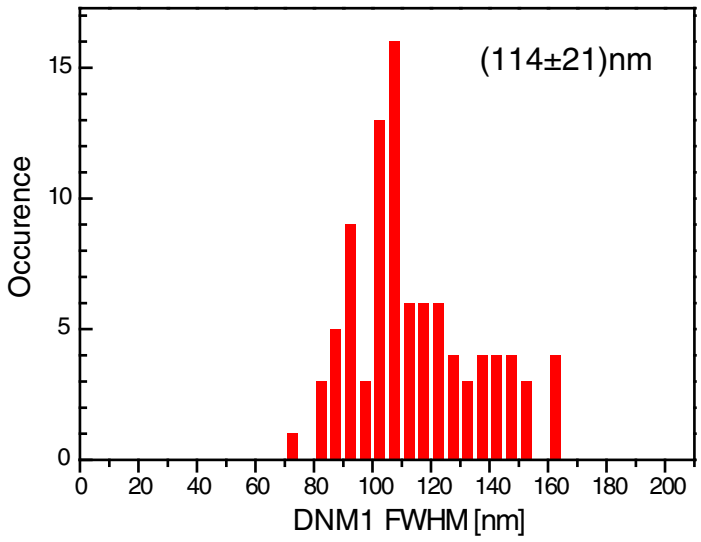


**Figure 4.5:** Size distribution of Dnm1p spots on yeast mitochondria. The value denotes the mean ± standard deviation.

more than twice as high as the standard deviation for the VLP-GFP measurement shown in Fig. 4.2. As the fluorescence signal of the Dnm1p-clusters was rather larger than that for the VLP-GFP particles, this broadening can not be explained by photon statistics and therefore must be due to a large size distribution of the cluster.

There are different possibilities which have to be considered: First, the size of the effective PSF might be slightly broader if the particle is not perfectly located in the focal plane. This effect is small as the depth of focus is very high (compare Chapter 2.1.2) and as only the brightest spots were evaluated. Second, it was shown by 3-D confocal imaging that the brightness variation of the Dnm1p cluster is larger than for the VLP1 [86]. This is an indication that the Dnm1p clusters not always include the same amount of protein Dnm1p-GFP and therefore are expected to vary in size. Third, the distribution may be broadened due to clustering or ring formation as described before. A ring of 109 nm diameter imaged by an effective PSF of 70 nm FWHM would reveal a spot of 182 nm FWHM. Since the ring could have any orientation in the three dimensional yeast cell, all values between 182 nm and the size of the effective PSF are to be expected. This explanations fit with the measured broad distribution. Small values would reflect that the thin ring is oriented approximately perpendicular to the imaging surface. Although the ring formation is expected to happen rarely (about 1 ring out of 50 Dnm1p clusters [86]), there can still be intermediate states in which the proteins start to crawl around the mitochondria.

One should note that the determination of object sizes depends highly on their shape. Simulations show (data not shown) that a sphere of 100 -110 nm diameter completely filled by the dye, imaged by an effective PSF of 70 nm FWHM, would result in a spot size of 114 nm FWHM. This would correlate with the average values obtained for the Dnm1p clusters shown in Fig. 4.5. Whereas a ring of similar diameter results in a much larger

spot size of 182 nm.

Summarizing, there are evidences that the Dnm1p is not only assembled into small, spherical clusters. Careful STED imaging could be a possibility to resolve the ring structure of Dnm1p in yeast mitochondria.

# 5 Conclusion and outlook

This thesis presents the extension of STED microscopy to the visible range and as a result first applications to solve problems in cell biology. The examples demonstrate that there is a broad range of applications for which sub-diffraction light microscopy opens up new insights. Especially with the availability of visible dyes instead of the barely visible far-red to infrared dyes used before, sample inspection has become much easier as samples can be visually checked in standard widefield or confocal microscopes. The yellow-green emitting dye Atto532 was introduced as a first fluorophore conjugated with STED in the visible range. It can be employed for immunolabeling as was demonstrated by the recording of membrane microdomains and a synaptic vesicle protein. As was further shown, the same dye may also be used to stain colloidal particles. Even the use of GFP, meanwhile a well-established probe with a rapidly increasing number of applications in biology, was demonstrated to be compatible with STED. This can be considered a milestone in the advancement of STED microscopy because it opens up the whole field of biology and may even allow for live cell imaging in the future.

The first application presented in this thesis was the imaging of syntaxin and SNAP-25 microdomains. These are only two examples of a whole family of different proteins of the plasma membrane [46]. The well-resolved microdomains demonstrate the potential of the STED microscopy in the research on membrane microdomains. Currently, the formation of membrane microdomains is of upmost interest, demonstrated by the fact that the initial publication postulating the raft hypothesis [47] has been cited more than 1200 times since 1997. In principle, every type of microdomain containing rafts may be imaged by STED providing that the staining is reliable. For example, while rafts are clearly defined in-vitro, they are hard to detect in-vivo as they lack clear morphological features, necessitating the use of a combination of markers [13].
The resolution of 65 nm achieved using the Atto532 immunolabeling of the microdomains was restricted (i) by the limited laser power available and (ii) by the imperfection of the doughnut's zero. An improvement of the focal zero by adaptive optics is currently under investigation.

The second application addressed the question whether synaptic vesicles remain patched after exocytosis, a problem not addressable using other methods. The resolution of a confocal microscope is not sufficient as can be seen in the control images and the labeling efficiency for EM is not adequate. The STED images of vesicles before and after fusion recorded here indeed confirmed that they remain patched after exocytosis.

The STED images of virus-like particles (VLP) containing GFP molecules proved the applicability of fluorescent proteins as a marker in STED microscopy. As a first exam-

ple of a real-world application, images of protein clusters in yeast mitochondria were recorded and evaluated. In this particular example, the use of a genetically encoded marker was mandatory because mitochondrial proteins can usually not be immunolabeled like the proteins in the previous examples. Using GFP as a marker, live cell imaging with STED can be considered in the future.

To render the STED microscope applicable for live cell imaging, some further developments have to be done. First, the oil immersion lens must be replaced by water immersion objectives to match the refractive index of the aqueous environment required for live cells. Second, the image recording time is too slow to image live cells which are inevitably moving. This goal can be addressed by implementing a beam scanning scheme instead of the stage scanning used here. It might be even necessary to parallelize the STED microscope by implementing multiple sub-diffraction focal spots. It should be pointed out, though, that smaller focal volumes come at the expense of a refined scanning (smaller pixel size) of the sample. That is, to accumulate the same amount of photons per area, the imaging of a cell (or a portion of it) will inevitably take longer with a STED microscope compared to a confocal one. Further, the photon stability of GFP might be improved by mutagenesis to get a better signal-to-noise ratio of the GFP images. Therefore, all of the available proteins should be tested for STED efficiency and photostability. Because in most of the bleaching pathways the triplet state is involved [35] triplet quenchers such as ascorbic acid, cyclooctatetraene (COT), mercaptoethylamine (MEA) or n-propyl gallate (n-PG) might decrease the photobleaching.

Staining of two different targets in one and the same cell with two different colors is very common in biological light microscopy. Commercial light microscopes are even capable of recording two or more colors in a single scan. Two colors are, for instance, used to localize proteins within the cell. For example, it has been shown in a two-color experiment that the Dnm1p fission protein in yeast is indeed localized on the yeast mitochondria. Another common example is the counterstaining of the nucleus to ensure that the cell is alive or to track the cell's state within the cell cycle. To tune a STED microscope towards two-color operation, a first, easy-to-implement step would be to image just one color using STED and the other color only in the confocal mode (for example the DAPI stained nucleus). The requirements for a full-featured two-color STED microscope are more advanced because two high-power lasers are necessary.

While it has been shown in this thesis that a subdiffraction resolution in two dimensions is well sufficient for many applications, the ultimate goal is clearly a 3-D sub-diffraction microscope. Just as with the multicolor option, the way to go is conceptually clear and is likely to be realized in the near future.

# Bibliography


[1] B. Alberts, D. Bray, J. Lewis, M. Raff, K. Roberts, and J.D. Watson. *Molekularbiologie der Zelle*. VCH, Weinheim; New York; Basel; Cambridge; Tokyo, 3. aufl. edition, 1995.

[2] E. Abbe. Beiträge zur theorie des mikroskops und der mikroskopischen wahrnehmung. *Arch. f. Mikr. Anat.*, 9:413–420, 1873.

[3] C. Gerthsen and H. Vogel. *Gerthsen Physik*, volume 18. Springer, Berlin, Heidelberg, 1995.

[4] J. Frank, T. Wagenknecht, B. F. McEwen, M. Marko, C. E. Hsieh, and C. A. Mannella. Three-dimensional imaging of biological complexity. *Journal of Structural Biology*, 138(1-2):85–91, 2002.

[5] W. Baumeister. Electron tomography: towards visualizing the molecular organization of the cytoplasm. *Current Opinion in Structural Biology*, 12(5):679–684, 2002.

[6] James F. Hainfeld and Richard D. Powell. New frontiers in gold labeling. *J. Histochem. Cytochem.*, 48(4):471–480, 2000.

[7] G. Gaietta, T. J. Deerinck, S. R. Adams, J. Bouwer, O. Tour, D. W. Laird, G. E. Sosinsky, R. Y. Tsien, and M. H. Ellisman. Multicolor and electron microscopic imaging of connexin trafficking. *Science*, 296(5567):503–507, 2002.

[8] B. J. Trask. Human cytogenetics: 46 chromosomes, 46 years and counting. *Nature Reviews Genetics*, 3(10):769–778, 2002.

[9] D. C. Prasher, V. K. Eckenrode, W. W. Ward, F. G. Prendergast, and M. J. Cormier. Primary structure of the aequorea-victoria green-fluorescent protein. *Gene*, 111(2):229–233, 1992.

[10] R. Y. Tsien. The green fluorescent protein. *Annual Review of Biochemistry*, 67:509–544, 1998.

[11] J. Lippincott-Schwartz and G. H. Patterson. Development and use of fluorescent protein markers in living cells. *Science*, 300(5616):87–91, 2003. Review.

[12] B. A. Griffin, S. R. Adams, and R. Y. Tsien. Specific covalent labeling of recombinant protein molecules inside live cells. *Science*, 281(5374):269–272, 1998.

[13] B. C. Lagerholm, G. E. Weinreb, K. Jacobson, and N. L. Thompson. Detecting microdomains in intact cell membranes. *Annual Review of Physical Chemistry*, 56:309–336, 2005.

[14] E. A. Jares-Erijman and T. M. Jovin. Fret imaging. *Nature Biotechnology*, 21(11):1387–1395, 2003. 739AL.

[15] M. A. Hink, T. Bisseling, and Ajwg Visser. Imaging protein-protein interactions in living cells. *Plant Molecular Biology*, 50(6):871–883, 2002.

[16] P. Schwille, U. Haupts, S. Maiti, and W. W. Webb. Molecular dynamics in living cells observed by fluorescence correlation spectroscopy with one- and two-photon excitation. *Biophysical Journal*, 77(4):2251–2265, 1999.

[17] D. Axelrod, D. E. Koppel, J. Schlessinger, E. Elson, and W. W. Webb. Mobility measurement by analysis of fluorescence photobleaching recovery kinetics. *Biophysical Journal*, 16(9):1055–1069, 1976.

[18] M. Minsky. Microscopy apparatus, 1961.

[19] S. W. Paddock. Confocal laser scanning microscopy. *Biotechniques*, 27(5):992–1004, 1999.

[20] T. Wilson (ed.). *Confocal microscopy*. Academic Press Ltd., London, 1990.

[21] S. Inoue. Foundation of confocal scanned imaging in light microscopy. In J.B. Pawley, editor, *Handbook of Biological Confocal Microscopy*, pages 1–17. Penum Press, New York, 2nd ed. edition, 1995.

[22] S. W. Hell and E. H. K. Stelzer. Fundamental improvement of resolution with a 4pi-confocal fluorescence microscope using two-photon excitation. *Opt. Commun.*, 93:277–282, 1992.

[23] S. W. Hell, M. Dyba, and S. Jakobs. Concepts for nanoscale resolution in fluorescence microscopy. *Curr. Opin. Neurobio.*, 14(5):599–609, 2004.

[24] H. Gugel, J. Bewersdorf, S. Jakobs, J. Engelhardt, R. Storz, and S.W. Hell. Cooperative 4pi excitation and detection yields 7-fold sharper optical sections in live cell microscopy. *Biophys. J.*, 87:4146–4152, 2004.

[25] F. de Lange, A. Cambi, R. Huijbens, B. de Bakker, W. Rensen, M. Garcia-Parajo, N. van Hulst, and C. G. Figdor. Cell biology beyond the diffraction limit: near-field scanning optical microscopy. *Journal of Cell Science*, 114(23):4153–4160, 2001.

[26] W. Denk, J.H. Strickler, and W. W. Webb. Two-photon laser scanning fluorescence microscopy. *Science*, 248:73–76, 1990.

[27] K. Konig. Multiphoton microscopy in life sciences. *Journal of Microscopy-Oxford*, 200:83–104, 2000. Part 2.

[28] W. R. Zipfel, R. M. Williams, and W. W. Webb. Nonlinear magic: multiphoton microscopy in the biosciences. *Nature Biotechnology*, 21(11):1368–1376, 2003. 739AL.

[29] S.W. Hell and J. Wichmann. Breaking the diffraction resolution limit by stimulated emission:stimulated emission depletion microscopy. *Opt. Lett.*, 19(11):780–782, 1994.

[30] S.W. Hell. Toward fluorescence nanoscopy. *Nature Biotechnol.*, 21(11):1347–1355, 2003.

[31] V. Westphal and S.W. Hell. Nanoscale resolution in the focal plane of an optical microscope. *Phys. Rev. Lett.*, 94:143903, 2005.

[32] S. W. Hell. Increasing the resolution of far-field fluorescence light microscopy by point-spread-function engineering. In J.R. Lakowicz, editor, *Topics in Fluorescence Spectroscopy*, volume 5, pages 361–422. Plenum Press, New York, 1997.

[33] H. Haken and H.C. Wolf. *Molekülphysik und Quantenchemie*. Springer, Berlin Heidelberg New York, 3. aufl. edition, 1998.

[34] M. Dyba, J. Keller, and S. W. Hell. Phase filter enhanced sted-4pi fluorescence microscopy: theory and experiment. *New Journal of Physics*, 7, 2005.

[35] M. Dyba and S.W. Hell. Photostability of a fluorescent marker under pulsed excited-state depletion through stimulated emission. *Appl. Optics*, 42(25):5123–5129, 2003.

[36] S.W. Hell and M. Kroug. Ground-state depletion fluorescence microscopy, a concept for breaking the diffraction resolution limit. *Appl. Phys. B*, 60:495–497, 1995.

[37] M. Hofmann, C. Eggeling, S. Jakobs, and S. W. Hell. Breaking the diffraction barrier in fluorescence microscopy at low light intensities by using reversibly photoswitchable proteins. *PNAS*, 102(49):17565–17569, 2005.

[38] T.A. Klar and S.W. Hell. Subdiffraction resolution in far-field fluorescence microscopy. *Opt. Lett.*, 24(14):954–956, 1999.

[39] M. Dyba and S.W. Hell. Focal spots of size l/23 open up far-field fluorescence microscopy at 33 nm axial resolution. *Phys. Rev. Lett.*, 88:163901, 2002.

[40] M. Dyba, S. Jakobs, and S.W. Hell. Immunofluorescence stimulated emission depletion microscopy. *Nature Biotechnol.*, 21(11):1303 – 1304, 2003.

[41] T. A. Klar, S. Jakobs, M. Dyba, A. Egner, and S. W. Hell. Fluorescence microscopy with diffraction resolution limit broken by stimulated emission. *Proc. Natl. Acad. Sci. USA*, 97:8206–8210, 2000.

[42] Y. Igasaki, F. H. Li, N. Yoshida, H. Toyoda, T. Inoue, N. Mukohzaka, Y. Kobayashi, and T. Hara. High efficiency electrically-addressable phase-only spatial light modulator. *Optical Review*, 6(4):339–344, 1999.

[43] J. Keller, A. Schönle, and S.W. Hell. In preparation. 2006.

[44] Fan Yang, Larry G. Moss, and George N. Phillips. The molecular structure of green fluorescent protein. 14(10):1246–1251, 1996. TY - JOUR 10.1038/nbt1096-1246.

[45] J. Zhang, R. E. Campbell, A. Y. Ting, and R. Y. Tsien. Creating new fluorescent probes for cell biology [review]. *Nature Reviews Molecular Cell Biology*, 3(12):906–918, 2002. Using Smart Source Parsing Dec.

[46] F. R. Maxfield. Plasma membrane microdomains. *Current Opinion in Cell Biology*, 14(4):483–487, 2002. TY - JOUR.

[47] K. Simons and E. Ikonen. Functional rafts in cell membranes. *Nature*, 387(6633):569–572, 1997.

[48] T. Lang, D. Bruns, D. Wenzel, D. Riedel, P. Holroyd, C. Thiele, and R. Jahn. Snares are concentrated in cholesterol-dependent clusters that define docking and fusion sites for exocytosis. *Embo Journal*, 20(9):2202–2213, 2001.

[49] R. Jahn. Principles of exocytosis and membrane fusion. In *Gastroenteropancreatic Neuroendocrine Tumor Disease: Molecular and Cell Biological Aspects*, volume 1014 of *Annals of the New York Academy of Sciences*, pages 170–178. 2004.

[50] R. Jahn, T. Lang, and T. C. Sudhof. Membrane fusion. *Cell*, 112(4):519–533, 2003.

[51] R. B. Sutton, D. Fasshauer, R. Jahn, and A. T. Brunger. Crystal structure of a snare complex involved in synaptic exocytosis at 2.4 angstrom resolution. *Nature*, 395(6700):347–353, 1998.

[52] P. Holroyd, T. Lang, D. Wenzel, P. De Camilli, and R. Jahn. Imaging direct, dynamin-dependent recapture of fusing secretory granules on plasma membrane lawns from pc12 cells. *PNAS*, 99(26):16806–16811, 2002.

[53] J. Avery, D. J. Ellis, T. Lang, P. Holroyd, D. Riedel, R. M. Henderson, J. M. Edwardson, and R. Jahn. A cell-free system for regulated exocytosis in pc12 cells. *J. Cell Biol.*, 148(2):317–324, 2000.

[54] T. Lang. Imaging snares at work in 'unroofed' cells - approaches that may be of general interest for functional studies on membrane proteins. *Biochemical Society Transactions*, 31:861–864, 2003. Part 4.

[55] P. Kask, K. Palo, D. Ullmann, and K. Gall. Fluorescence-intensity distribution analysis and its application in biomolecular detection technology. *Proceedings of the National Academy of Sciences of the United States of America*, 96(24):13756–13761, 1999.

[56] P. Kask, C. Eggeling, K. Palo, Ü. Mets, M. Cole, and K. Gall. Fluorescence intensity distribution analysis (fida) and fluorescence fluctuation techniques: theory and practice. In A. Kraayenhof, A. J. W. G. Visser, and H. C. Gerritsen, editors, *Fluorescence Spectroscopy, Imaging and Probes*, volume 2, pages 153–181. Springer Verlag, Berlin, Heidelberg, New York, 2002.

[57] L. Kastrup, H. Blom, C. Eggeling, and S. W. Hell. Fluorescence fluctuation spectroscopy in subdiffraction focal volumes. *Physical Review Letters*, 94(17), 2005.

[58] N. O. Petersen. Fcs and spatial correlations on biological surfaces. In R. Rigler and E.S. Elson, editors, *Fluorescence Correlation Spectroscopy*, volume 65 of *Chemical Physics*, pages 162–184. Springer, Berlin, Heidelber, New York, 2001.

[59] P. Kask and K. Palo. Introduction to the theory of fluorescence intensity distribution analyis. In R. Rigler and E.S. Elson, editors, *Fluorescence Correlation Spectroscopy:Theory and Applications*, volume 65, pages 396–409. Springer, Berlin, Heidelberg, New York, 2001.

[60] E. L. Elson and D. Magde. Fluorescence correlation spectroscopy .1. conceptual basis and theory. *Biopolymers*, 13(1):1–27, 1974.

[61] N. O. Petersen. Scanning fluorescence correlation spectroscopy .1. theory and simulation of aggregation measurements. *Biophysical Journal*, 49(4):809–815, 1986.

[62] N. O. Petersen, P. L. Hoddelius, P. W. Wiseman, O. Seger, and K. E. Magnusson. Quantitation of membrane-receptor distributions by image correlation spectroscopy - concept and application. *Biophysical Journal*, 65(3):1135–1146, 1993.

[63] T. Lang, M. Margittai, H. Holzler, and R. Jahn. Snares in native plasma membranes are active and readily form core complexes with endogenous and exogenous snares. *Journal of Cell Biology*, 158(4):751–760, 2002.

[64] J.S. Sieber, K.I. Willig, R. Heintzmann, S. W. Hell, and T. Lang. The snare-motif is essential for syntaxin-clusterin in the plasma membrane. (submitted), 2005.

[65] D. A. Brown and J. K. Rose. Sorting of gpi-anchored proteins to glycolipid-enriched membrane subdomains during transport to the apical cell-surface. *Cell*, 68(3):533–544, 1992.

[66] T. C. Sudhof. The synaptic vesicle cycle. *Ann. Rev. Neurosci.*, 27:509–547, 2004.

[67] B. Ceccarel, W. P. Hurlbut, and A. Mauro. Turnover of transmitter and synaptic vesicles at frog neuromuscular junction. *J. Cell Biol.*, 57(2):499–524, 1973.

[68] J. E. Heuser and T. S. Reese. Evidence for recycling of synaptic vesicle membrane during transmitter release at frog neuromuscular junction. *J. Cell Biol.*, 57(2):315–344, 1973.

[69] E. R. Chapman and R. Jahn. Calcium-dependent interaction of the cytoplasmic region of synaptotagmin with membranes - autonomous function of a single c-2-homologous domain. *J. Biol. Chem.*, 269(8):5735–5741, 1994.

[70] K. Kraszewski, O. Mundigl, L. Daniell, C. Verderio, M. Matteoli, and P. Decamilli. Synaptic vesicle dynamics in living cultured hippocampal-neurons visualized with cy3-conjugated antibodies directed against the lumenal domain of synaptotagmin. *J. Neuroscience*, 15(6):4328–4342, 1995.

[71] N. Brose, A. G. Petrenko, T. C. Sudhof, and R. Jahn. Synaptotagmin - a calcium sensor on the synaptic vesicle surface. *Science*, 256(5059):1021–1025, 1992.

[72] J. L. Pyle, E. T. Kavalali, E. S. Piedras-Renteria, and R. W. Tsien. Rapid reuse of readily releasable pool vesicles at hippocampal synapses. *Neuron*, 28(1):221–231, 2000.

[73] K. M. Harris and P. Sultan. Variation in the number, location and size of synaptic vesicles provides an anatomical basis for the nonuniform probability of release at hippocampal ca1 synapses. *Neuropharmacology*, 34(11):1387–1395, 1995.

[74] S. Sankaranarayanan and T. A. Ryan. Real-time measurements of vesicle-snare recycling in synapses of the central nervous system. *Nature Cell Biol.*, 2(4):197–204, 2000.

[75] Thilo Hofmann. Kolloide: Die welt der vernachlässigten dimensionen. *Chemie in unserer Zeit*, 38(1):24–35, 2004.

[76] N. A. M. Verhaegh, J. S. Vanduijneveldt, A. Vanblaaderen, and H. N. W. Lekkerkerker. Direct observation of stacking disorder in a colloidal crystal. *Journal of Chemical Physics*, 102(3):1416–1421, 1995.

[77] A. van Blaaderen. Imaging individual particles in concentrated colloidal dispersions by confocal scanning light-microscopy. *Advanced Materials*, 5(1):52–54, 1993.

[78] M. E. Leunissen, C. G. Christova, A. P. Hynninen, C. P. Royall, A. I. Campbell, A. Imhof, M. Dijkstra, R. van Roij, and A. van Blaaderen. Ionic colloidal crystals of oppositely charged particles. *Nature*, 437(7056):235–240, 2005.

[79] A. M. Alsayed, M. F. Islam, J. Zhang, P. J. Collings, and A. G. Yodh. Premelting at defects within bulk colloidal crystals. *Science*, 309(5738):1207–1210, 2005.

[80] P. Jiang, J. F. Bertone, K. S. Hwang, and V. L. Colvin. Single-crystal colloidal multilayers of controlled thickness. *Chemistry of Materials*, 11(8):2132–2140, 1999.

[81] A. Charpilienne, M. Nejmeddine, M. Berois, N. Parez, E. Neumann, E. Hewat, G. Trugnan, and J. Cohen. Individual rotavirus-like particles containing 120 molecules of fluorescent protein are visible in living cells. *J. Biol. Chem.*, 276(31):29361–29367, 2001.

[82] D. Otsuga, B. R. Keegan, E. Brisch, J. W. Thatcher, G. J. Hermann, W. Bleazard, and J. M. Shaw. The dynamin-related gtpase, dnm1p, controls mitochondrial morphology in yeast. *J. Cell Biol.*, 143(2):333–349, 1998.

[83] K. Okamoto and J. M. Shaw. Mitochondrial morphology and dynamics in yeast and multicellular eukaryotes. *Annual Review of Genetics*, 39(1):503–536, 2005.

[84] E. Ingerman, E. M. Perkins, M. Marino, J. A. Mears, J. . McCaffery, J. E. Hinshaw, and J. Nunnari. Dnm1 forms spirals that are structurally tailored to fit mitochondria. *J. Cell Biol.*, 170(7):1021–1027, 2005.

[85] K. L. Cerveny and R. E. Jensen. The wd-repeats of net2p interact with dnm1p and fis1p to regulate division of mitochondria. *Molecular Biology of the Cell*, 14(10):4126–4139, 2003.

[86] A. C. Schauss, J. Bewersdorf, and S. Jakobs. Fis1p and caf4p, but not mdv1p, determine the polar localization of dnm1p clusters on the mitochondrial surface. *submitted*, 2006.

[87] K. Osseoasare and F. J. Arriagada. Preparation of sio2 nanoparticles in a nonionic reverse micellar system. *Colloids and Surfaces*, 50:321–339, 1990.

[88] F. J. Arriagada and K. Osseo-Asare. Synthesis of nanosize silica in a nonionic water-in-oil microemulsion: Effects of the water/surfactant molar ratio and ammonia concentration. *Journal of Colloid and Interface Science*, 211(2):210–220, 1999.

[89] G. H. Bogush, M. A. Tracy, and C. F. Zukoski. Preparation of monodisperse silica particles - control of size and mass fraction. *Journal of Non-Crystalline Solids*, 104(1):95–106, 1988.

[90] A. van Blaaderen and A. Vrij. Synthesis and characterization of colloidal dispersions of fluorescent, monodisperse silica spheres. *Langmuir*, 8(12):2921–2931, 1992.

# A Appendix

## A.1 Membrane microdomains: material and methods

*Cell culture*
PC12 cells (clone 251; Heumann et al, 1983) were maintained, propageted and transfected as described in [48] apart from the following modifications. For overexpression the cells were transfected with 20 - 40 $\mu$g of plasmid. The PC12 cells were prepared for experiments approximately 48 hrs after transfection.

*Primary antibodies*
Monoclonal antibodies were used for the detection of syntaxin 1 (HPC-1, Barnstable et al., 1985) and SNAP-25 (clone Cl 71.1; Bruns et al.,1997).

*Secondary antibody*
sheep anti-mouse IgGs (Cat# 515-005-003, Dianova) were labeled with Atto532 (provided by K.H. Drexhage, Department of Chemistry, University of Siegen, Germany) via it´s succinimidyl ester.

*sheet preparation*
Membrane sheets were prepared as described (Avery et al., 2000) and [48]. In brief, cells were grown on poly-L-lysine coated coverslips and disrupted by a 100 ms ultrasound-treatment in ice-cold sonication-buffer (20 mM Hepes, pH 7.2, 120 mM potassium glutamate, 20 mM potassium acetate and 10 mM EGTA). Freshly prepared membrane sheets were fixed for 90-120 min at RT in $4\%$ paraformaldehyde (PFA) in PBS (137 mM NaCl and 8.1 mM $Na_2HPO_4$, pH 7.3) and immunostained. Then, they were mounted in Mowiol and imaged.

*single antibody controll*
Poly-L-lysine coated coverslips were fixed in 4% PFA and incubated with the primary antibody for 1-1.5 hrs. After carfull washing, it was incubated with the secondary antibody of the same concentration used for the images for 1-1.5 hrs. After washing, they were mounted in Mowiol.

# A.2 Synaptic vesicles

## A.2.1 Simulation of patched synaptic vesicles

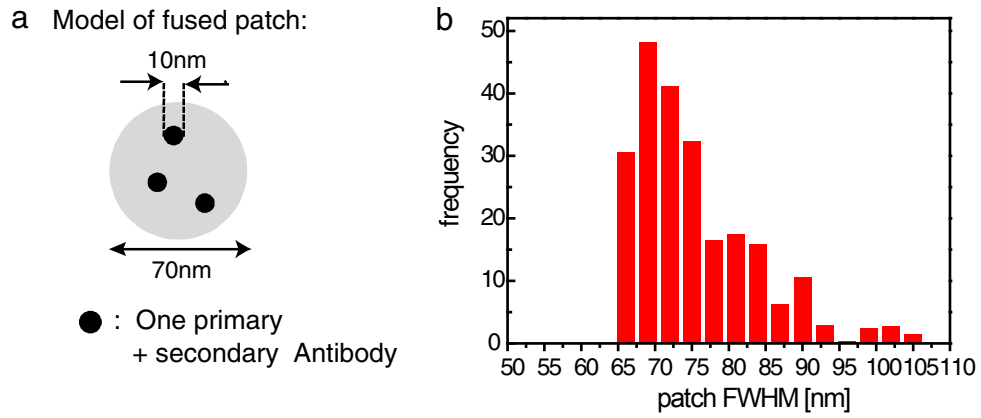


**Figure A.1:** Simulation of patched synaptic vesicle. a) Distribution of antibody-tagged synaptotagmin within a patch. b) Histogram of FWHM derived from simulated patches assuming random distribution of synaptotagmin within a patch and assuming a effective STED PSF of 65 nm.

## A.2.2 Material and methods

*Primary hippocampal neurons*

The cultures were prepared from newborn rats according to previously published protocols (Rosenmund and Stevens, 1997; Klingauf et al., 1998) and were used between 15 and 25 days in vitro. Both cultures plated onto astrocytic monolayers and cultures plated directly onto the coverslips were used, with identical results. For antibody labeling the neurons were incubated with a solution of anti-synaptotagmin monoclonal antibodies (604.1, Chapman et al., 1994) for 5 minutes at either 37°C or on ice (for selective surface staining) in a Tyrode solution containing 124 mM NaCl, 5 mM KCl, 2 mM $CaCl_2$, 1 mM $MgCl_2$, 30 mM glucose and 25 mM HEPES (pH 7.4), washed briefly and fixed with 4% paraformaldehyde in PBS containing 1mM EGTA. When indicated, the cultures were stimulated in presence of anti-synaptotagmin antibodies, at 37°C, in normal buffer containing calcium, prior to fixation. Surface-selective staining was then achieved by applying the secondary antibodies in absence of permeabilization. After washing, sheep anti-mouse Atto 532-labeled antibodies ware added for 2 hours at room temperature; the cultures were then mounted in Mowiol and imaged. Permeabilization was achieved by using 0.1% Triton X-100 after fixation. The use of monoclonal antibodies, rather than polyclonal ones, ensures that any molecular patch observed cannot result from antibady-induced clustering.

For investigation of the signal coming from single primary antibodies, poly-L-lysin treated coverslips were incubated with anti-synaptotagmin antibodies for 30 min, fixed, washed,

incubated with secondary antibodies and mounted in Mowiol.
The monoclonal antibody 41.1 was used to label the cytoplasmic domain of synaptotagmin (Brose et al., 1992)

## A.3 Microtubules: material and methods

The cells were grown on a coverslip and fixed with cold methanol. Their microtubules were labeled with a mouse anti-$\beta$-tubulin monoclonal antibody. The secondary antibody was used as previously described.

## A.4 Synthesis of colloidal particles

*Synthesis of particles via microemulsion technique:*
The non-fluorescent cores were synthesized in a water in oil microemulsion as described [87, 88]. The particle size was 52 nm diameter, characterized by TEM

*Coupling dye-APS:*
A mass of 1 milligram (1,3 $\mu$mol) of ATTO-532 NHS and 1 $\mu$l (about 3x equivalents) of APS ([3-Aminopropyl]triethoxysilane) were dissolved in 300 $\mu$l of absolute ethanol freshly distillated. The mixture was stirred and allowed to react overnight in the dark.

*Growing a fluorescent shell onto the beads:*
The total amount of dye-APS reacted overnight were used to grow a fluorescent shell onto beads of 52 nm diameter previously prepared [89, 90]. The amount of TES(Tetraethyl orthosilicate) was selected to grow the particles to a theoretical diameter of 65 nm. The ratio TES/dye is about 300. The experimental diameter measured by TEM is 68 nm.

*Growing a second non-fluorescent shell:*
A similar process without a fluorescent dye was used to grow a second shell onto the particles. The amount of TES was selected to grow the particles to a theoretical diameter of 130 nm. The experimental diameter measured by TEM is 132 nm.

## A.5 Miscellaneous

*Mowiol*
6 g Glycerol AR (#4094, Merck, Darmstadt, Germany), 2.4 g Mowiol 4-88 (Hoechst, Germany), 6 ml water, 12 ml 0.2M Tris ph 7.2 buffer)

*PBS: phosphate buffered saline*
10$\times$ stock solution: 80.0g NaCL, 2.0g KCl, 14.4g $Na_2HPO_4$, 2.4g $KH_2PO_4$,
1000 ml Aqua. dest., adjust pH with HCl

# Acknowledgments

This thesis was prepared in the department of NanoBiophotonics at the Max-Planck-Institute for Biophysical Chemistry in Göttingen. I would like to thank all people who have contributed to the success of this thesis. It was a joy to see STED growing up from its infancy to the first practical use in biology.

Prof. Dr. Stefan W. Hell not only proposed the fascinating project of STED applications but also provided an outstanding scientific environment. His continuous input of new ideas have significantly contributed to the success of this thesis.

Prof. Dr. J. Bille for his interest and being the second referee of this thesis.

This work of bridging the gap between high end microscopy technology and sophisticated biology would not have been possible without collaborators of high expertise and dedication.

- Jochen Sieber and Dr. Thorsten Lang, Department of Neurobiology
- Dr. Silvio Rizzoli and Prof. Dr. R. Jahn, Department of Neurobiology
- Dr. Stefan Jakobs, Sylvia Löbermann, and Rita Schmitz-Salue
- Astrid Schauß
- and all the biologists of the group of NanoBiophotonics for introducing a physicist to the world of biology.

Dr. Marcus Dyba for his assistance during my first two years and being a pleasant partner in the lab.

Dr. Christian Eggeling and Dr. Lars Kastrup for advice in FFS and for kindly proof-reading the manuscript.

Dr. Marianno Bossi, cook of the beads.

For valuable discussions and/or providing of software many thanks to Jan Keller, Robert Kellner, Dr. Andreas Schönle, and Dr. Volker Westphal.

Jaydev Jethwa for always offering assistance and proof-reading english manuscripts, even on the weekend.

This work would not have been possible without a great mechanical and optical workshop.

Last but not least, I want to thank my parents for their continuous support and for always being there.

Göttingen, december 2005

# List of publications

Parts of this thesis have been or will be published as follows

1. K.I. Willig, S. Rizzoli, V. Westphal, R. Jahn and S.W. Hell. STED-microscopy reveals that synaptotagmin remains clustered after synaptic vesicle exocytosis. *Nature*, in press.

2. J.J. Sieber, K.I. Willig, R. Heintzmann, S.W. Hell and T. Lang. The SNARE-motif is essential for syntaxin-clustering in the plasma membrane. Submitted to *Biophysical Journal*.

3. R.J. Kittel, C. Wichmann, T.M. Rasse, W. Fouquet, M. Schmidt, A. Schmid, D. Wagh, R.R. Kellner, K.I. Willig, S.W. Hell, E. Buchner, M. Heckmann, and S.J. Sigrist. The *Drosophila* Bruchpilot protein is required for presynaptic active zone assembly and calcium-channel clustering to ensure high vesicle release probability. Submitted to *Nature*.

4. S.W. Hell, M. Dyba, S. Jakobs, K.I. Willig, L. Kastrup and V. Westphal. Nanoscale resolution with focused light: STED and other RESOLFT microscopy concepts. In J.B. Pawley, editor, *Handbook of Biological Confocal Microscopy*, 3. edition, 2006, in press